



Ben-Gurion University of the Negev
The Faculty of Engineering Sciences
The Department of Software and Information Systems Engineering

Cell-context dependent in silico organelle localization in label-free microscopy images

Thesis submitted in partial fulfillment of the requirements
for the Master of Sciences degree

Nitsan Elmalam

Under the supervision of **Prof. Assaf Zaritsky**

September 2024




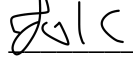
Ben-Gurion University of the Negev
The Faculty of Engineering Sciences
The Department of Software and Information Systems Engineering

Cell-context dependent in silico organelle localization in label-free microscopy images

Thesis submitted in partial fulfillment of the requirements
for the Master of Sciences degree

Nitsan Elmalam

Under the supervision of **Prof. Assaf Zaritsky**

Author:		20.09.2024
Supervisor:		20.09.2024
Chairman of Graduate Studies Committee:	_____	_____

September 2024

Abstract

In silico labeling prediction of organelle fluorescence from label-free microscopy images has the potential to revolutionize our understanding of cells as integrated complex systems. However, changes in the intracellular organization across cell types, throughout biological processes and perturbations, can lead to altered label-free images and impaired in silico labeling. We demonstrated that incorporating biological meaningful cell contexts, via a context-dependent model that we call CELTIC, enhanced in silico labeling prediction and enabled downstream analysis of out-of-distribution cell populations such as cells undergoing mitosis, and cells located at the edge of the colony. These results suggest a link between cell context and intracellular organization. Using CELTIC for generative traversal along single cells undergoing context transition enabled integrated characterization of the gradual alterations in cellular organization across multiple organelles, overcoming inter-cell variability. The explicit inclusion of context has the potential to harmonize multiple datasets, paving the way for generalized in silico labeling foundation models.

Acknowledgments

I would like to express my deepest gratitude to my supervisor, Prof. Assaf Zaritsky, for his exceptional mentorship. His patient guidance, enthusiasm for new ideas, and encouragement of free thinking and innovation have been invaluable throughout this journey. I am also grateful to Lion Ben Nedava for guiding me through the initial steps of my research and always offering wise advice. Special thanks to Matheus Viana and Jianxu Chen from the Allen Institute for collaborating with us and offering thoughtful suggestions. To my children - Maya, Noam, and Ella - thank you for your patience and love during the many weekends and late nights of absence. Finally, my deepest thanks to my partner, Michal, who was not only a keen biological advisor to my many questions but also walked alongside me through every moment of this journey.

Contents

Abstract	3
Acknowledgments	4
Contents	5
List of Figures & Tables	6
Introduction	7
Related Work	9
In silico labeling	9
Fusing image and tabular data	10
Results	11
Deteriorated in silico labeling for rare cell populations	11
CELTIC, cell-context dependent in silico labeling	15
Cell-context contributes to the in silico labeling of rare cell populations	17
Predicting spindle axis in mitotic cells enabled by CELTIC	20
Context-dependent generative organelle localization with CELTIC	23
Discussion	27
Methods	29
Data	29
In silico labeling replication	29
Single cell models image preprocessing	30
Context Representations	30
CELTIC architecture	31
CELTIC training and test analysis	32
Ablation study	33
Spindle prediction	33
Using context for image generation	33
Supplementary Information	35
References	46
תקציר	53

List of Figures & Tables

Figure 1	Inferior in silico labeling for rare cell populations	13
Figure 2	CELTIC - incorporating the cell context to the in silico labeling models	16
Figure 3	Qualitative and quantitative assessment of CELTIC's contribution to the in silico labeling of rare cell populations	18
Figure 4	Application-appropriate downstream analysis: in silico prediction of the spindle axis location and orientation	21
Figure 5	In silico labeling generation of variable cellular contexts	25
Figure S1	Distribution of single cell in silico labeling performance across organelles for rare cell populations	35
Figure S2	CELTIC architecture	36
Figure S3	Ablation study showing the impact of different context types on in silico labeling of rare cell populations	37
Table S1	Results of replicating the U-Net-based in silico labeling model as reported in (Ounkomol et al. 2018)	38
Table S2	In silico labeling accuracy analysis in rare cell populations	39
Table S3	Comparison of single-cell in silico labeling accuracy between rare populations with context (CELTIC) and without context (U-NET)	41
Table S4	Ablation study on the contribution of each context type to in silico labeling of rare populations	43

Introduction

Organelles act in concert to shape and enable cell function. Accordingly, the organization of organelles and the spatial relations between different organelles are remarkably versatile and can change in response to multitude factors including undergoing cellular processes such as proliferation (Carlton et al. 2020), migration (Kroll and Renkawitz 2024) or differentiation (Lee et al. 2018; Ahmed et al. 2022), and being influenced by extrinsic factors such as local cell density and different microenvironmental conditions (e.g., mechanical stresses, diffusible factors, chemical treatments) (Miroshnikova and Wickström 2022; Ye et al. 2023). For instance, during mitosis, the nuclear envelope disassembles, the nucleus undergoes condensation and separation, the Golgi apparatus is disassembled and then reformed, and microtubules rearrange to form the mitotic spindle (Carlton et al. 2020). The ability to measure whether and how the intracellular organization of organelles change is fundamental to cell biology but is technically challenging due to substantial limitations in simultaneous labeling of multiple organelles within the same cell (Garini et al. 2006).

In silico labeling of organelles is the computational cross-modality translation of label-free transmitted light microscopy images to their corresponding organelle-specific fluorescent images (Elmalem et al. 2024). In silico labeling holds the promise of enabling computationally multiplexed live cell imaging toward an integrated understanding of the cell (Sullivan and Lundberg 2018). Attaining an in silico labeling model involves the acquisition of matched label-free and fluorescently labeled images, and using them to train a deep learning model that maps the label-free images to their corresponding matched fluorescence images (Ounkomol et al. 2018). This training process is repeated for each organelle, producing a set of organelle-specific in silico labeling models (Fig. 1A, left). At inference, the organelle-specific models can be applied to generate a multiplexed image displaying the localization of several organelles simultaneously (Cheng et al. 2021) (Fig. 1A, right). Several recent studies demonstrated that in silico labeling can be applied to reveal how the intracellular organelle organization, cell shape and/or cell behavior alters in response to different cell states and different experimental conditions (Christiansen et al. 2018; Kandel et al. 2020; Cheng et al. 2021; Kandel et al. 2021; Jo et al. 2021; Ben-Yehuda et al. 2022; Gu et al. 2022; Cross-Zamirski et al. 2022; Somani et al. 2022; Wang et al. 2023; Noy et al. 2023; Atwell et al. 2023; Asmar et al. 2024; Ivanov et al. 2024; Liu et al. 2024). This forthcoming wave of in silico labeling applications to cell phenotyping raises a major question regarding generalization: are in silico labeling models confounded by cells that are not sufficiently represented during training? In principle, changes in the intracellular organization can alter the cell's optical properties, inducing out-of-distribution label-free images and impaired in silico labeling. For example,

alterations in the cell's internal organization due to changes in cell-cell adhesions in densely packed microenvironments may lead to changes in the cell's optical properties that in turn can hamper high quality in silico labeling. Indeed, a few studies demonstrated inferior performance upon perturbations (Jo et al. 2021) or upon inference on a cell type different from the one seen on training (Tonks et al. 2024). This deteriorated accuracy in organelle localization is posing a limitation in generalizing in silico labeling and hampering the possibility of using in silico labeling to understand how intracellular organelle organization is changing across cell types, throughout biological processes and following perturbations.

Here we focus on the problem of out-of-distribution label-free images due to rare cellular states and contexts that are under-represented in the training data. We report a decreased performance of in silico labeling for rare cell populations, and introduce a new method called CELL in silico Labeling using Tabular Input Context, or CELTIC, to overcome this limitation. CELTIC improves in silico labeling of rare cell populations by incorporating biological meaningful cell context (encoded as tabular data) to the in silico labeling model. We show that by inclusion of cell context CELTIC enhances the in silico labeling of rare cell populations, especially organelle localization patterns associated with that context. We demonstrate that CELTIC has the potential to reveal alterations in intracellular organization between different cell contexts.

Related Work

In silico labeling

Monitoring multiple organelles simultaneously is crucial for understanding cellular interaction networks (Valm et al., 2017). However, limitations in imaging techniques - such as photo-toxicity during extended imaging periods, photobleaching, and constraints on the number of distinguishable parallel stain channels due to overlapping fluorophore emissions - hinder comprehensive analyses of cellular heterogeneity and dynamics (Garini et al., 2006; Icha et al., 2017). In 2018, in silico labeling was introduced as a deep learning method that transforms label-free microscopy images into synthetic fluorescent images of specific organelles, thus enabling long-term, multi-organelle imaging while overcoming these limitations (Christiansen et al., 2018; Ounkomol et al., 2018). Since its introduction, in silico labeling has been adapted and extended to a variety of organelles, cell types, and imaging modalities, such as for organelle segmentation in electron microscopy data (Heinrich et al., 2021) and for transforming phase images of tissue slides into pathologically stained images (Rivenson, Liu, et al., 2019).

In silico labeling is referred to by various terms, including 'augmented microscopy' and 'virtual staining' (Z. Wang et al., 2021). It has been successfully applied to cell tracking (Pylvänäinen et al., 2023) and segmentation (Heinrich et al., 2021), particularly for nuclear and membrane marker predictions from label-free images. This approach enables analyses of cell motility (Atwell et al., 2023), shape dynamics, and behavior under different experimental conditions, including differentiation and viral infection (Ivanov et al., 2024). The technique has proven effective in both 2D and 3D cultures (X. Chen et al., 2023), even with low-resolution images (LaChance & Cohen, 2020). Moreover, in silico labeling demonstrates great potential in high-content phenotypic screening (Cross-Zamirski et al., 2022), DNA fragmentation analysis in sperm cells (Noy et al., 2023), live-cell phenotyping during viral infection (Ivanov et al., 2024), long-term tracking of cellular growth (Kandel et al., 2020), mitochondrial dynamics (Somani et al., 2022), and the inference of cell types and states (Christiansen et al., 2018).

The accuracy of in silico labeling models varies across organelles. High-quality predictions have been reported for organelles such as the nuclei and lipid droplets while some organelles such as the Golgi apparatus and microtubules suffer from poor quality (Elmalam et al., 2024). Even with high accuracy, in silico labelling is not error free. Thus, the full potential of the technique is currently constrained by partial accuracies and the influence of prediction errors on downstream analyses. To improve in silico

labeling accuracy, several studies have employed advanced deep learning architectures, including attention based models (Rivenson, Wang, et al., 2019; Z. Wang et al., 2021), generative adversarial networks (Cross-Zamirski et al., 2022) and multitask learning (Christiansen et al., 2018), though the gains remain modest. Quantitative phase imaging, a label-free imaging modality, holds promise for enhancing in silico labeling by providing more organelle-specific optical contrast (Park et al., 2023). Additionally, there is a growing discourse on transitioning from pixel-based correlation and reconstruction error metrics to application-specific evaluation metrics (LaChance & Cohen, 2020). This paper demonstrates an example of such a metric for spindle axis prediction, which could better assess the biological relevance of labeling outcomes.

Fusing image and tabular data

Integrating image and tabular data within a single neural network often involves concatenating the latent space of the image with a vector representation of the tabular data, followed by a linear layer for tasks such as classification (Pölsterl et al., 2020). An alternative, although less efficient, approach employs a two-step process in which the latent representations from a convolutional neural network are input to a separate network designed solely for the tabular data (Li et al., 2019). Conversely, more advanced techniques allow for nonlinear contributions from the tabular data by integrating multiple layers with activation functions (Mobadersany et al., 2018). However, these methods are prone to overfitting and may suffer from low quality as they primarily interact with the global image descriptor through concatenation, as noted in (Wolf et al., 2022).

(Mati, 2015) trains a network that learns a scalar from the tabular data, which is then utilized to rescale the image feature maps. (Perez et al., 2018) enhances this technique by adding a shifting of the feature map, for visual reasoning and question-answering tasks. (Wolf et al., 2022) further developed this integration with the Dynamic Affine Feature Map Transform (DAFT), which effectively fuses tabular data with brain MRI images. DAFT has been employed by (Płotka et al., 2023) to predict fetal birth weight by merging fetal ultrasound video scans with clinical data. In (White et al., 2024) it was applied to fuse demographic and clinical characteristics with MRI images for predicting post-stroke symptoms. (Rickmann et al., 2023) used DAFT to incorporate prior information regarding gallbladder resection with MRI feature maps to improve segmentation accuracy.

Results

Deteriorated in silico labeling for rare cell populations

We used 3D spinning-disk microscopy images of genetically edited fluorescent human induced pluripotent stem cell lines (hiPSC) colonies from the Allen Institute for Cell Science (AICS) WTC-11 hiPSC Single-Cell Image Dataset v1 (Viana et al. 2023). The dataset comprises 3D field of view images, each containing label-free (brightfield), and a specific genetically edited EGFP-tagged protein representing an organelle. In addition, the dataset contains cell segmentation masks and metadata regarding the individual cells, that includes annotations regarding the cell cycle stage (interphase / prophase / early prometaphase / prometaphase-metaphase / anaphase-telophase-cytokinesis), and its location within a colony (interior / edge). We decided to focus on six organelles that span the range of in silico labeling performances reported in (Ounkomol et al. 2018). Organelles with high performance in silico labeling included the nuclear envelope, actin filaments, and microtubules (average pixel-wise Pearson correlation coefficient of $\sim 0.78-0.88$), organelles with intermediate performance included the mitochondria and endoplasmic reticulum ($\sim 0.66-0.73$), and organelles with low performance included the Golgi apparatus (0.23). We replicated the U-Net-based (Ronneberger et al. 2015) in silico labeling model reported in (Ounkomol et al. 2018) and reproduced their results (Table S1).

Our focus on the context of the single cell, required us to use the cells' segmentation masks to isolate individual cells, and assign for each cell whether it was undergoing mitosis (non-dividing - interphase, or one of five mitotic stages), its location in the colony (whether it is located at the colony's interior or edge), its volume, and its local density (i.e., number of adjacent neighboring cells in the colony). Overall we collected a single cell dataset consisting of 1,116-1,575 single cells per organelle, extracted from 100 fields of view images that were never seen by the trained model for each organelle. Cells in interphase accounted for more than 95% of the cells in our dataset, cells located away from the colony's edge accounted for over 98%, cells with typical volumes (i.e., z-score higher than -1.5 relative to the overall population distribution) accounted about 93%, and cells in microenvironment of typical density (i.e., 5 or more adjacent neighbors) accounted for about 96% (Fig. 1B, Table S2). For each cell we measured the Pearson's correlation coefficients (PCC) between the fluorescent ground truth and its corresponding in silico prediction. Overlaying a field of view PCC values onto the single cell segmentation masks showed poor endoplasmic reticulum in silico labeling for two cells in the prometaphase/metaphase stage of mitosis and for another cell located in a sparse neighborhood (Fig. 1C). Similarly, cells in prometaphase/metaphase and early prometaphase stages of mitosis showed poor

in silico labeling for the nuclear envelope (Fig. 1D). To systematically evaluate this observation, we pooled all single cell PCC values across organelles and rare populations (Table S2). Cells undergoing mitosis displayed declined in silico labeling across all organelles compared to cells in interphase (Fig. 1E). The most dramatic performance deterioration occurred for microtubules and for the nuclear envelope. Cells located at the colony edge exhibited inferior in silico labeling of the microtubules and actin (Fig. S1 A). Cells with small volumes and cells in sparse microenvironments demonstrated reduced in silico labeling for most organelles, and most prominently for the nuclear envelope and actin (Fig. S1 B-C). These results underscore the inherent challenge of applying in silico labeling to rare cell populations, likely due to out-of-distribution intracellular organization and the corresponding changes in these cells' optical properties. We hypothesize that incorporating context information about each cell will increase the performance of in silico label models and address the generalizability issue of these models to under-represented data.

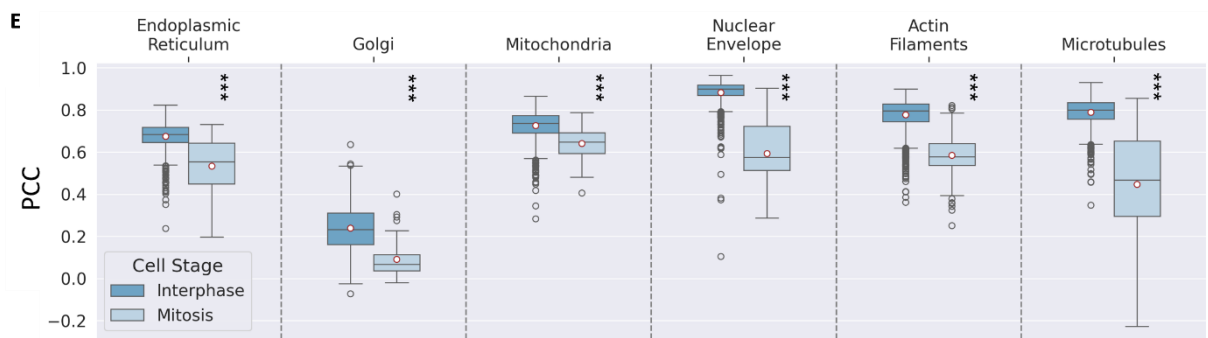
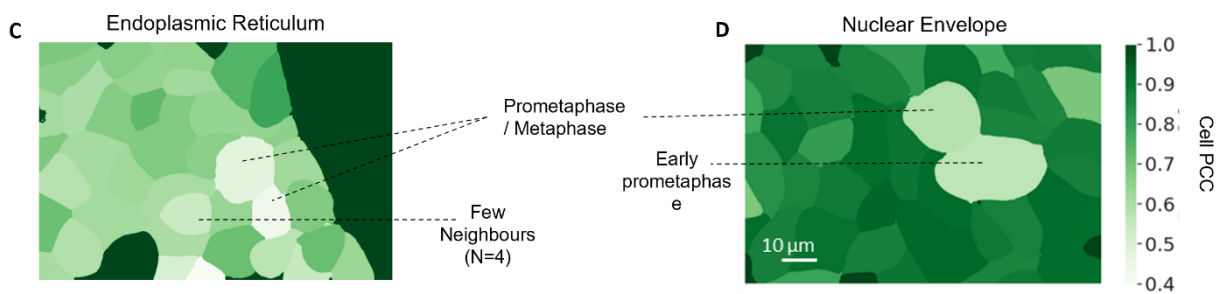
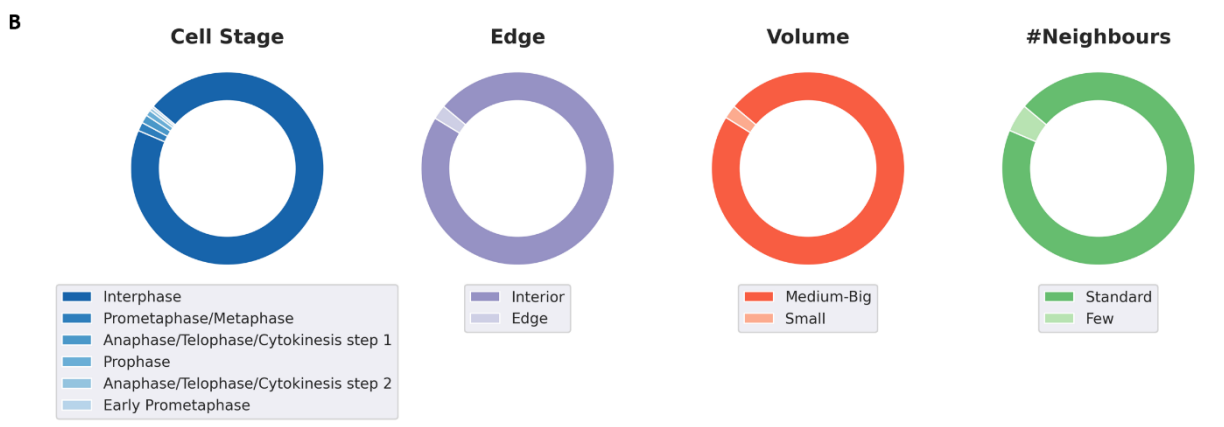
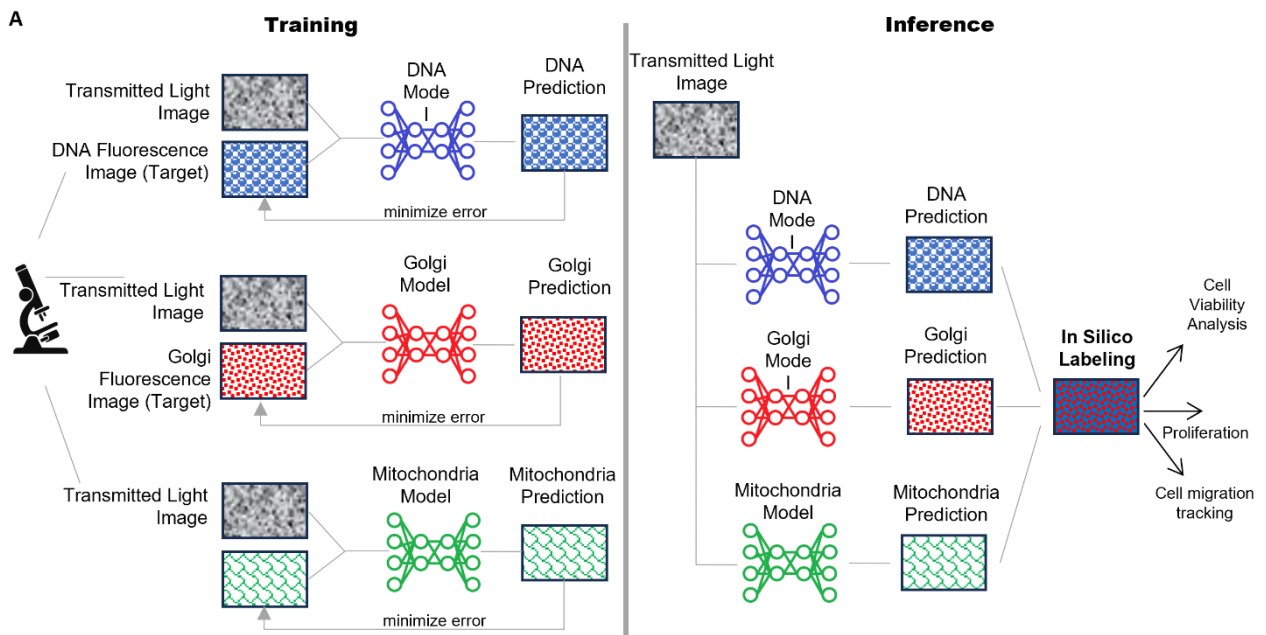


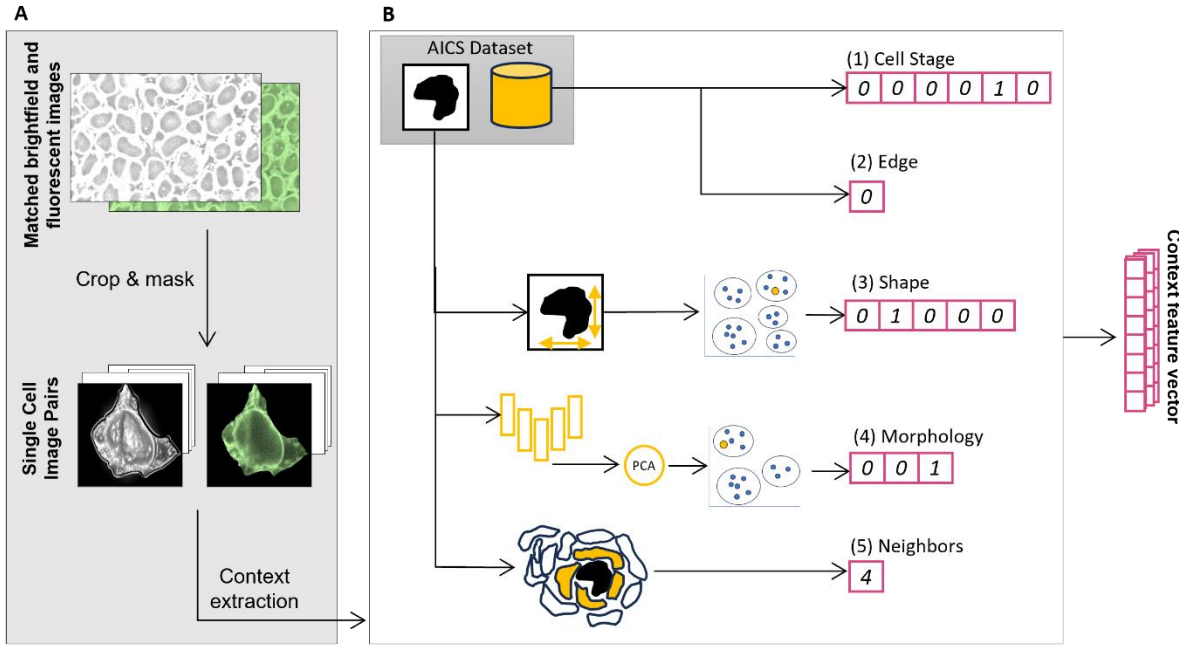
Figure 1. Inferior in silico labeling for rare cell populations. (A) In silico labeling. Training (left): an organelle-specific model receives label-free transmitted light images and their corresponding fluorescent targets and is trained to minimize the reconstruction error between the model's prediction and the target. Inference (right): each organelle-specific model translates a label-free image to its corresponding predicted fluorescence image. The predictions can be combined to an integrated multi-organelle image, which can be used for downstream analyses. (B) Distribution of rare cell populations in the dataset across a mixed population of six organelles, comprising 7,622 single cells. Left to right: Cell Stage: cells in interphase constitute >95% of the total population. The remaining 5 mitotic stages were distributed among the remaining 5%; Edge: 2.4% of cells were located at the colony edge; Volume: 2.2% of the cells had z-score lower than -1.5 relative to the population distribution; #Neighbors: 4.7% of the cells had few (4 or less) neighbors. (C and D) Cellular-level prediction accuracy label maps. Each colored region in the field of view (FOV)-based label map represents the replicated U-Net's (Ounkomol et al. 2018) average Pearson correlation coefficient of a cell. Scale bar = 10µm. (C) Two cells in the prometaphase/metaphase stage of mitosis and one cell with a few neighbors with poor in silico labeling of the endoplasmic reticulum. (D) Two cells in the prometaphase/metaphase and early prometaphase stages of mitosis with poor in silico labeling of the nuclear envelope. (E) Distribution of single cell in silico labeling performance across organelles for cells in interphase (dark blue) versus mitosis (light blue). Mann-Whitney U test *** - p-values < 0.001. Full results including in silico labeling performance, statistical tests and population sizes are available in Table S2.

CELTIC, cell-context dependent in silico labeling

We propose CELTIC, an in silico labeling model that integrates cellular contextual information. CELTIC is an image-to-image translation model, where the innermost layer of the network (“bottleneck layer”) explicitly encodes predefined cell context parameters. The single cell centric approach required us to move from a field of view-based to a single cell-based in silico labeling (Fig. 2A). Specifically, we cropped single cells according to their corresponding fluorescent plasma membrane-derived segmentation masks. For this model, we transitioned to full-resolution z-slices ($y = 624$, $x = 924$), making direct comparison of the PCC metric with the initial model of (Ounkomol et al. 2018) infeasible (see Methods). We defined five types of context representations per cell (Fig. 2B). The first type of context was the mitotic state represented as a one-hot encoding vector. The second type was a binary indicator representing the cell’s position in the colony. The third and fourth context types encoded the cell’s shape and morphology. The third type was a one-hot encoded vector from k-means clustering ($k = 5$) of shape descriptors (height, min/max width, volume). The fourth type used an autoencoder to compress binary cell masks derived from segmentation images into lower-dimensional morphology representations. These compressed representations were then clustered using k-means ($k = 3$), and each cell was subsequently represented by a one-hot encoded vector corresponding to its morphology cluster membership. The rationale for these shape and morphology representations is outlined in the Methods. Finally, the fifth context representation was a scalar quantifying the local density as the number of adjacent cells. These five context representations were concatenated to define a 16-dimensional context feature vector encoding the single cell context.

CELTIC extends the classic U-Net architecture by incorporating the context vector to its deepest layer. We followed the footsteps of a recent method called DAFT (Wolf et al. 2022), that was previously applied with ResNet for classification tasks and more recently with U-Net for medical image segmentation (Rickmann et al. 2023). DAFT uses the cellular context vectors to affine-transform the bottleneck image representations (Fig. 2C, Fig. S2). In CELTIC, this approach enables the network to learn a unified representation that incorporates both the intrinsic image details encoded at the network deepest layer along with the contextual cellular information.

Context Extraction



Training

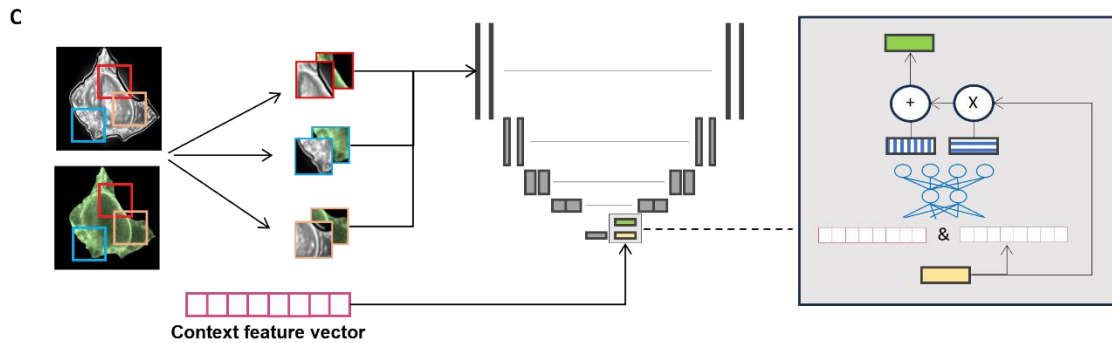


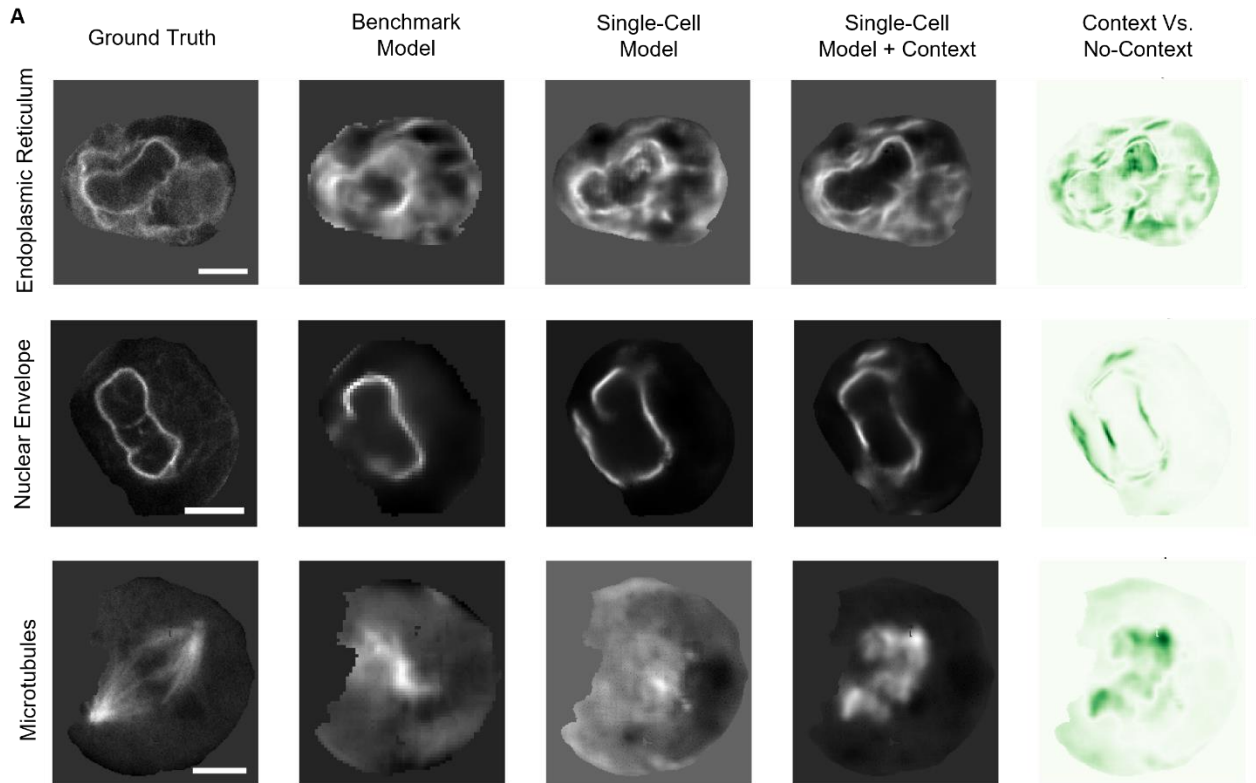
Figure 2. CELTIC - incorporating the cell context to the in silico labeling models. (A-B) Context extraction. (A) Single-cell images are cropped and masked. (B) Single cell context is extracted and represented by a 16-dimensional context feature vector, comprising five context types. The mitotic stage and the edge location indicator contexts were available in the AICS dataset's metadata, other contexts are computationally extracted from the segmented cells and concatenated to define the context feature vector (magenta). (C) CELTIC's architecture. Image patches are fed to CELTIC along with their corresponding context. The cell context is incorporated as an auxiliary input to the U-Net in silico labeling model transforming the U-Net's bottleneck layer (yellow) into a context-enriched feature map (green) via the DAFT (Wolf et al. 2022) block (gray box with a detailed view on the right). DAFT uses its own bottleneck to fuse the image and context, creating a scaler and shifter that adjust the feature map accordingly (see Methods and Fig. S2 for more details).

Cell-context contributes to the in silico labeling of rare cell populations

To evaluate the contribution of the cell's context we compared the single cell-based in silico labeling of rare cell populations trained without (U-NET) or with (CELTIC) context. For cells undergoing mitosis, inclusion of context contributed to better predictions of the endoplasmic reticulum and the nuclear envelope in dividing cells (Fig. 3A). Both models display poor performance in predicting microtubules mitotic spindle, but CELTIC was the only model that was able to predict the two astral arrays radiating from the spindle poles during mitosis (Fig. 3A). These subjective visual assessments were systematically confirmed by calculating the Δ PCC defined as the signed mean contribution of context to the single cell-based in silico labeling model, i.e., positive Δ PCC values indicate that the cell context contributed to the in silico prediction. Indeed, cell context enhanced the prediction of cells in mitosis for all organelles (Fig. 3B, Table S3). The most prominent contribution was measured for microtubules, which is expected given the dramatic changes occurring in microtubule organization during cell division. Similarly, inclusion of context improved the in silico labeling of cells at the colony edge, most notably for the Golgi apparatus and for microtubules (Fig. 3B). Cells with small volumes also showed improvement in most cases, particularly for the endoplasmic reticulum and for the nuclear envelope. Lastly, adding context enhanced the in silico prediction of cells in sparse neighborhoods, with the most substantial differences observed for the Golgi apparatus and for the nuclear envelope (Fig. 3B). Intriguingly, context systematically contributed to the in silico labeling of most organelles, even when considering the entire cell population (Fig. 3B, "All"), but this contribution was marginal because the rare populations constituted only a small fraction of the dataset. The models were trained on the original datasets without enrichment of rare populations, requiring the model to learn from the limited samples available. For instance, the endoplasmic reticulum dataset included only 28 mitotic cells out of 697 total training cells, with some subcategories, such as early prometaphase, containing as few as 2 cells.

To elucidate the contribution of each context type to the in silico labeling of rare populations, we conducted an ablation study. Specifically, we randomized each context type by shuffling the corresponding context values across the single cell population and measured the reduction in the in silico labeling with the shuffled context (Table S4). This analysis revealed that several context types were contributing to the in silico labeling of cells undergoing mitosis, unsurprisingly with cell stage ranking first among them (Fig. S3). The inclusion of the edge context predominantly impacted cells situated at the periphery of the colony for the in silico labeling of the endoplasmic reticulum, nuclear envelope and the microtubules. Cells with small volumes were primarily influenced by the shape and morphology contexts, particularly for the endoplasmic reticulum, Golgi apparatus, nuclear envelope, and actin. Intriguingly, the neighbor context had minimal effect on most rare populations. Overall, we conclude

that cell context, especially one that associates with a corresponding population, such as cell cycle stage for mitotic cells, contributes to in silico labeling by “guiding” representations that adapt to the different intracellular organizations associated with rare cell populations.



B

	Population				
	All	Mitosis	Edge	Small Volume	Few Neighbors
Endoplasmic Reticulum	0.01 ± 0.03 ***	0.01 ± 0.06	0.02 ± 0.09	0.03 ± 0.04 ***	0.02 ± 0.06 **
Golgi Apparatus	0.03 ± 0.08 ***	0.03 ± 0.05 ***	0.05 ± 0.05 ***	0.02 ± 0.10	0.03 ± 0.08 **
Mitochondria	0.00 ± 0.03 ***	0.01 ± 0.02 ***	0.00 ± 0.02	0.01 ± 0.03	0.00 ± 0.03
Nuclear Envelope	0.01 ± 0.03 ***	0.04 ± 0.09 **	0.01 ± 0.01 **	0.03 ± 0.06 *	0.02 ± 0.04 ***
Actin Filaments	0.00 ± 0.02	0.01 ± 0.04 **	0.00 ± 0.02	0.00 ± 0.03	0.00 ± 0.02
Microtubules	0.01 ± 0.09 ***	0.20 ± 0.31 ***	0.02 ± 0.04 ***	0.00 ± 0.03	0.01 ± 0.05 *

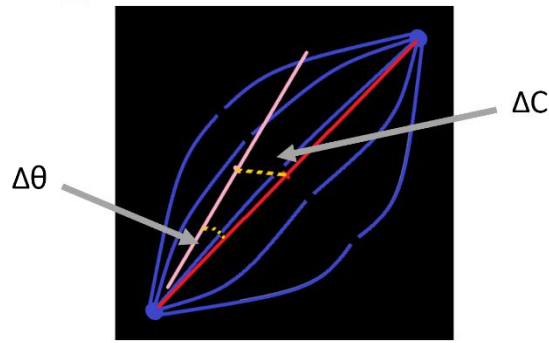
Figure 3. Qualitative and quantitative assessment of CELTIC’s contribution to the in silico labeling of rare cell populations. (A) In silico labeling visualization of mitotic cells. Each row visualizes a different organelle (top-to-bottom): endoplasmic reticulum of a cell in late mitosis, nuclear envelope of a cell in late mitosis, microtubules of a cell in the prometaphase/metaphase stage. Left-to-right: ground truth fluorescence, U-Net replicating (Ounkomol et al. 2018), single cell-based in silico

labeling (U-Net), CELTIC, the absolute pixel-wise difference between CELTIC and the single cell-based model. Darker regions mark bigger differences. Shown are Z slices that have been selected by an expert based on the ground truth full z-stack images. Scale bar = 5 μ m. **(B)** Quantification of the contribution of context, via CELTIC, to the in silico labeling of six organelles in the rare cell populations. Mean and standard deviation of the Δ PCC for each population and for each organelle. The entire population (left) for reference. Wilcoxon signed-rank test was used to reject the null hypothesis that Δ PCC is distributed around zero: * - $p < 0.05$, ** - $p < 0.01$, *** - $p < 0.001$. Full results are provided in Table S3.

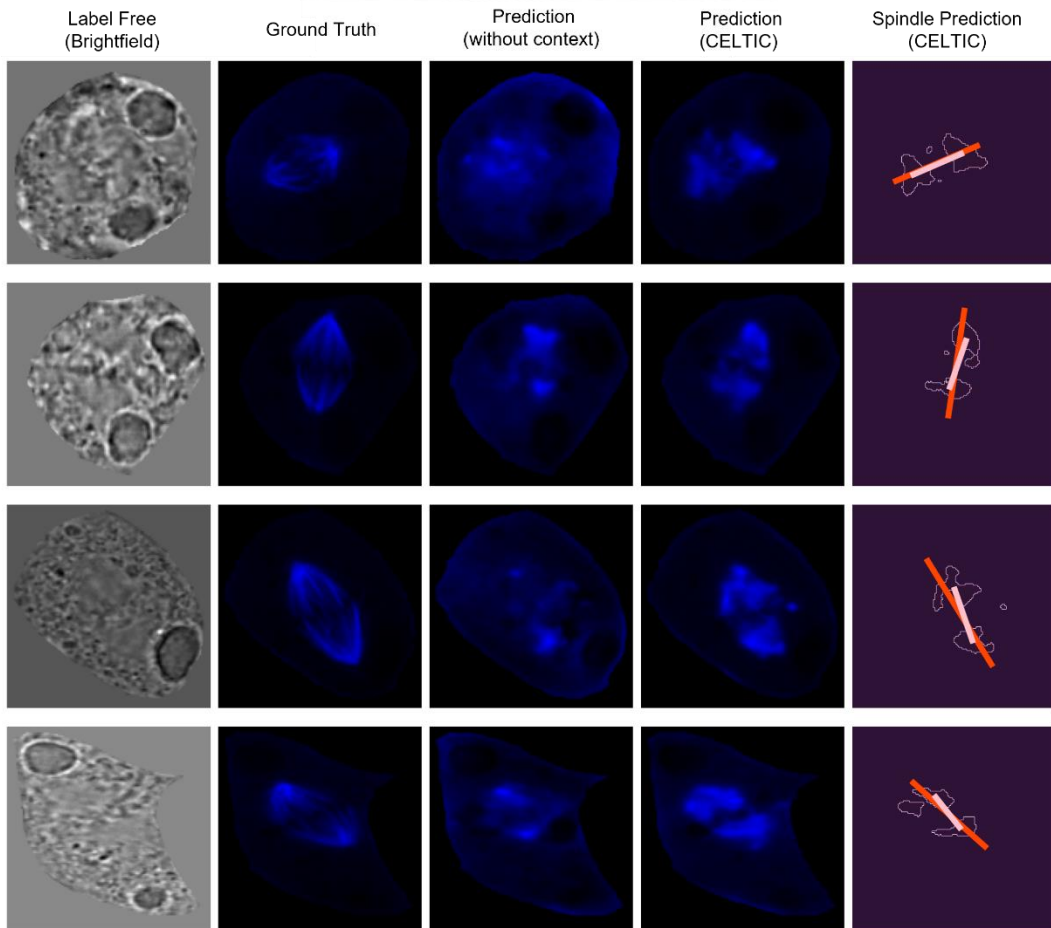
Predicting spindle axis in mitotic cells enabled by CELTIC

The performance of an *in silico* labeling model should be evaluated based on its performance for specific application-appropriate downstream analyses, such as organelle localization, counts, and shape (LaChance and Cohen 2020; Chen et al. 2023; Elmalam et al. 2024). During mitosis, the spindle axis connects the two centrosomes and is a critical determinant of cell division orientation and outcome (Yamashita 2009). We decided to focus on the application-appropriate downstream analysis of determining the location and orientation of the spindle axis during mitosis from label-free images. We applied the single cell-based *in silico* model for microtubules, without and with the mitotics state context, for a set of prometaphase/metaphase cells that had not been seen before by the model. For consistency, we selected the middle z-slice from each image stack and resized the images to a standard size. Next, we performed a threshold-based segmentation of the *in silico* labeling predictions and set a line connecting the centers of mass of the two main contours in the image as the predicted spindle axis (see Methods). We defined two measurements to evaluate the predicted spindle axis: (1) location error - the distance between the center of the ground truth spindle axis line and the center of the predicted line (ΔC), and (2) orientation error - the angle between these two lines ($\Delta\theta$) (Fig. 4A). Visual assessment indicated that while both models were not able to perfectly reconstruct the microtubules spindle axis, CELTIC was able to provide reasonable predictions regarding the spindle location and orientation (Fig. 4B). Quantification of ΔC and $\Delta\theta$ reported that the spindle axis was predicted by CELTIC with a median location error ΔC of 3.8 pixels (0.15-0.27 μm before resizing), and with a median orientation error $\Delta\theta$ of 13°. Comparison to the single cell-based model (without context) showed deterioration of over 2 fold in the predicted location (Fig. 4C) error and over 1.5 fold in the predicted orientation error (Fig. 4D). To confirm that these prediction errors were not achieved by chance we conducted a permutation test where we randomly shuffled all single cell predictions and calculated the median $\Delta\theta$ prediction errors across the shuffled population. This process was repeated 250,000 times and was used to calculate the statistical significance - the fraction of times that the permuted mean errors were smaller or equal to the observed (unpermuted) mean error, reaching statistical significance $p\text{-value} < 2e\text{-}5$ (Fig. 4E). These results suggest that the inclusion of cell context in CELTIC can enhance the *in silico* labeling of (application-appropriate) organelle localization patterns that are associated with that context.

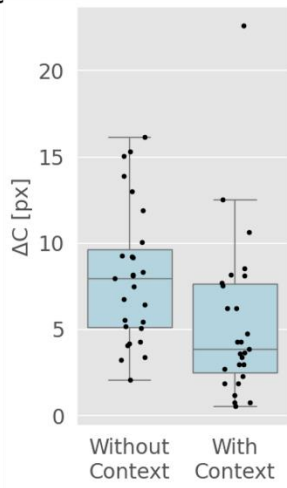
A



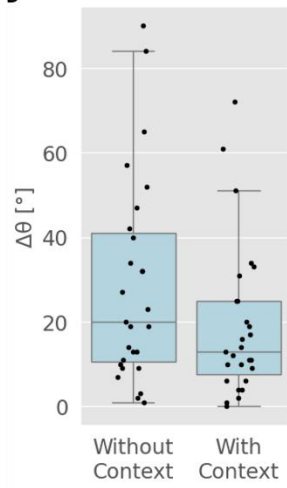
B



C



D



E

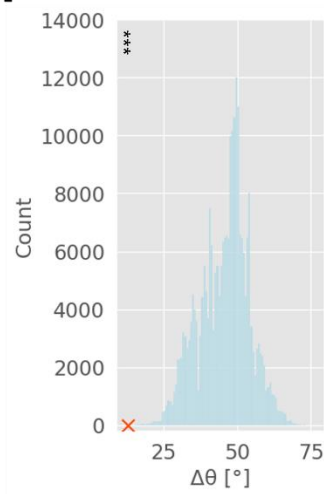


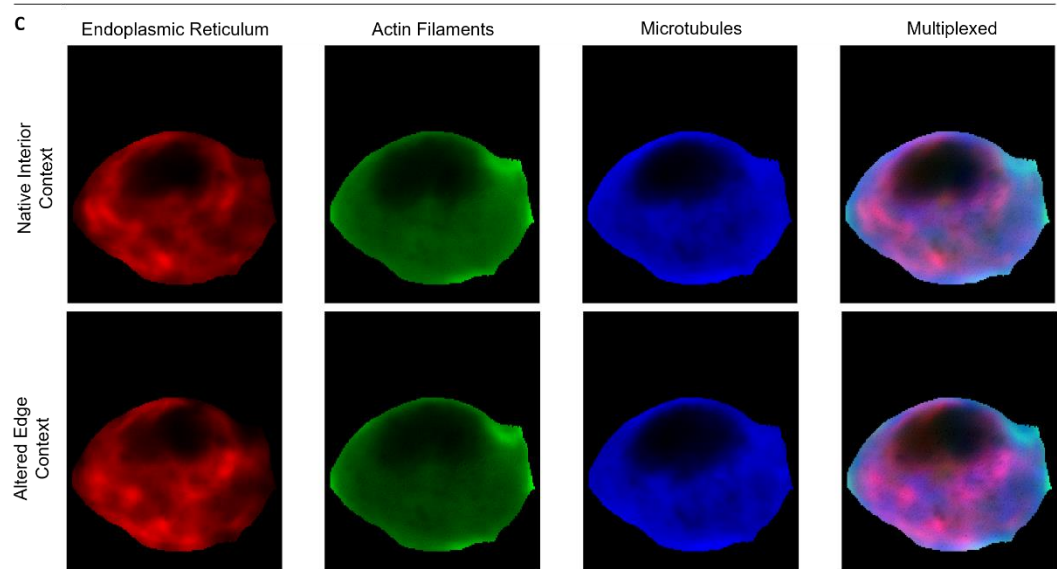
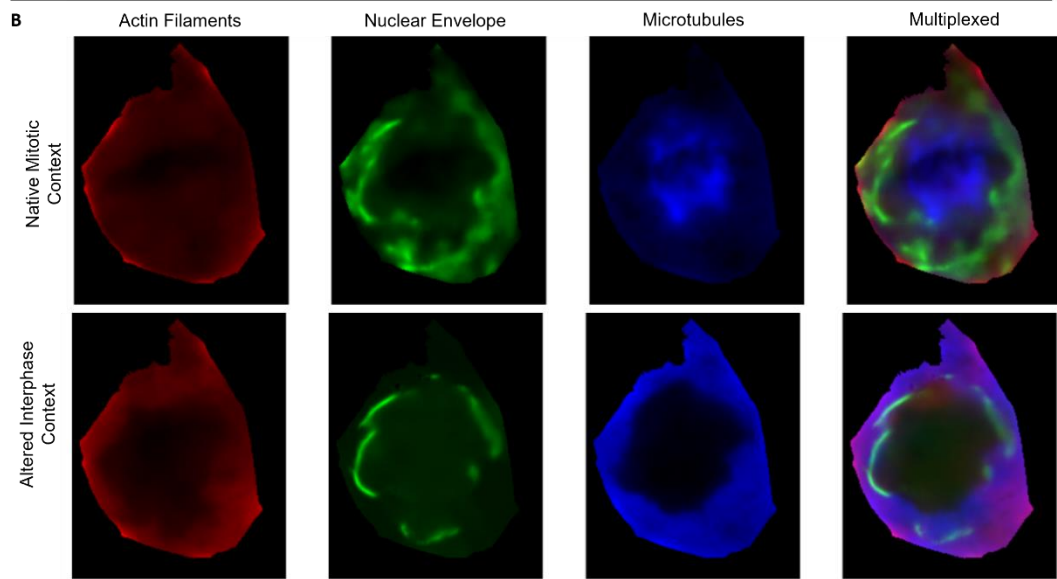
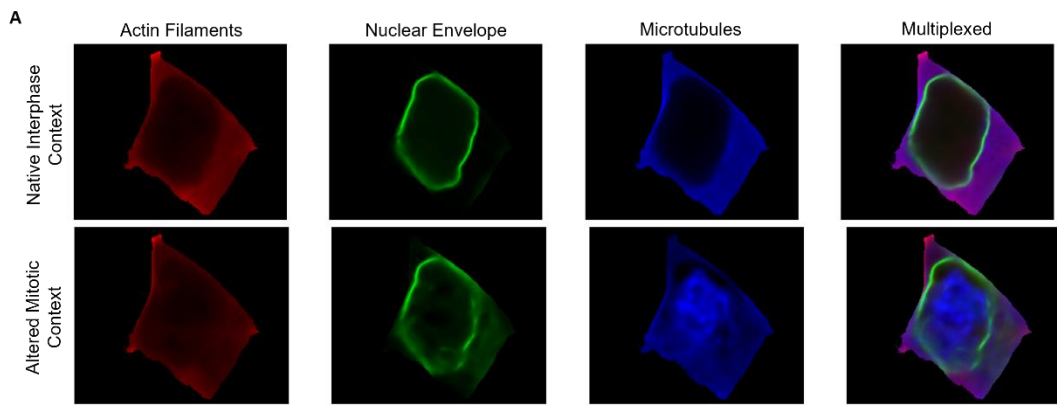
Figure 4. Application-appropriate downstream analysis: in silico prediction of the spindle axis location and orientation. (A) Measurements of the predicted spindle axis. The location error (ΔC) denotes the distance between the centers of the predicted (pink) and the ground truth (red) spindle axes. The orientation error ($\Delta\theta$) denotes the angle between the predicted and the ground truth spindle axes. (B) Four cells (rows) in the prometaphase/metaphase mitotic state. Columns represent (left-to-right): (i) brightfield label-free image; (ii) ground truth fluorescent microtubules image from the z-stack's middle slice; (iii) single cell-based model in silico labeling of microtubules ; (iv) CELTIC in silico labeling of microtubules; (v) Threshold-based segmentation of the CELTIC prediction, the spindle axis prediction (pink) and ground truth (red). In silico labeling was performed in 3D, while spindle axis prediction and segmentation were conducted in 2D. (C-D) Distribution of the location (C) and orientation (D) errors of the single cell-based versus CELTIC prediction of the spindle axis. Each data point corresponds to a single cell. (E) Permutation test: CELTIC's observed orientation error (red 'X', median $\Delta C = 13^\circ$) and the histogram of random shuffling (N=250,000).

Context-dependent generative organelle localization with CELTIC

The CELTIC representation incorporates the label-free image along with the cell context, which are jointly used to make the *in silico* prediction. This representation where the context can be manually manipulated can be used to generate a series of *in silico* labeling images of the same label-free image under varying contexts. To illustrate the potential of this approach, we generated the integrated *in silico* labeling of the actin filaments, the nuclear envelope and the microtubules of a non-dividing cell where the actin filaments and the microtubules formed widespread networks throughout the cytoplasm, with a solid nuclear envelope surrounding the nucleus (Fig. 5A, top). Upon manipulating the mitotic context, for the same label-free image, CELTIC generated an integrated *in silico* labeling where the actin filaments reorganized to form a ring at the cell equator in preparation for cytokinesis, the nuclear envelope broke down, and the microtubules reorganized to form the aligned mitotic spindle (Fig. 5A, bottom). Repeating the same process of context change and CELTIC generative organelle localization transitioning a cell from cell late mitosis to interphase produced an integrated *in silico* labeling resembling the interphase phenotype with dispersed actin filaments and microtubules and a more rigid-appearing nuclear envelope (Fig. 5B). As another demonstration, we used CELTIC to *in silico* label the endoplasmic reticulum, actin filaments and the microtubules of a cell located at the interior of the colony. Manipulating the edge context altered the localization of the endoplasmic reticulum from around the nucleus closer toward the cell's periphery (Fig 5C, top versus bottom), aligning with observations reported in (Viana et al. 2023) .

To systematically analyze how altering the cell's context changes the corresponding CELTIC-generated image, we manipulated each of the five context types, and calculated the Pearson correlation score between the generated image before and after the context alteration for 230 cells derived from 16 FOV images from the endoplasmic reticulum dataset (Fig. 5D). Altering the cell stage context made the most dramatic change in the generated image space, particularly for the microtubules and the Golgi apparatus. Alteration of the edge context was mapped to changes in the endoplasmic reticulum. Alteration of other contexts did not change the corresponding generated images. Given that CELTIC outperforms the single cell-based model that does not have access to the cell's context, these results suggest that CELTIC generalizes better for situations where there is no phenotypic difference or for scenarios where it recognizes its limited influence. Altogether, this analysis emphasizes that the CELTIC representation learns the cell's context, supporting its generalization to the rare cell population. The explicit representation of cell context also enables guided traversal along the context axis of the same cell, overcoming the vast variability between different cells. Analysis of the alteration in cell organization

along these context traversals may teach us about the gradual change in integrated cell state along a physiological process.



D

	Cell Stage	Edge	Shape	Morphology	Neighbors	PCC
Endoplasmic Reticulum	0.95	0.88	0.98	0.99	0.99	
Golgi	0.71	0.99	0.97	0.95	1.00	
Mitochondria	0.99	1.00	0.99	0.99	1.00	
Nuclear Envelope	0.88	0.98	0.99	1.00	1.00	
Actin Filaments	0.91	0.98	0.98	0.99	0.99	
Microtubules	0.52	0.95	0.99	0.99	1.00	

Figure 5. In silico labeling generation of variable cellular contexts. **(A)** In silico labeling of a cell in interphase. Top: The cell augmented with a native interphase context. Bottom: The cell augmented with a mitotic context. The images display the CELTIC results for the (left to right) actin filaments model (red), nuclear envelope model (green), microtubules model (blue), and a multiplexed representation of all three organelles together. **(B)** In silico labeling of a cell in prometaphase/metaphase. Top: The cell augmented with a native mitotic context. Bottom: The cell augmented with an interphase context. The descriptions of the images are analogous to those in panel A. **(C)** In silico labeling of a cell located far from the colony edge. Top: The cell augmented with a native interior context. Bottom: The cell augmented with a colony edge context. The images display the CELTIC results for the (left to right): endoplasmic reticulum model (red), actin filaments model (green), microtubules model (blue), and a multiplexed representation of all three organelles together. **(D)** Quantification of changes in CELTIC-generated images resulting from context alterations in the in silico labeling of six organelles, as predicted from images of 250 cells. Pearson Correlation Coefficient (PCC) was calculated between the original and altered images. Each cell in the table represents the mean PCC across the analyzed cells for the organelle (row) and the context type (column).

Discussion

Measuring and interpreting how organelles adjust their internal structure and organization in respect to one another under different experimental conditions or during a physiological process is the “holy grail” of cell biology. *In silico* labeling is a promising method to overcome some of the technical hurdles that currently prevent us from reaching this ultimate goal. Here, we report that *in silico* labeling is confounded by rare cell contexts due to alterations in the cells optical properties that lead to out-of-distribution label-free images. CELTIC guides context-dependent representations by incorporating the explicit cell context to the *in silico* labeling model. We show that CELTIC enhances the *in silico* labeling of rare cell populations, especially for organelle localization patterns associated with the corresponding context, and highlight its potential for modeling context-transitions through context-dependent generative capabilities. Our results emphasize the strong link between the cell’s context and its intracellular organization.

Cell context is a very broad term. It could be practically anything, from intrinsic cell contexts such as the ones shown in this study to extrinsic contexts such as the cell type, organelle, perturbations, disease state, assay, microscope, fluorescent marker and imaging parameters. The inclusion of context descriptors could be used to harmonize datasets from multiple resources to one large dataset. Thus context-dependent *in silico* labeling can be the enabler toward training general *in silico* labeling “foundation models”. Christiansen et al. made the first step in this direction by arguing for the benefit of training one model for the *in silico* labeling of multiple fluorescent channels (Christiansen et al. 2018). An exciting possibility is to integrate the cell’s continuous state during the progression of a physiological process as context for *in silico* labeling. For example, using the FUCCI system as rich cell cycle context (Sakaue-Sawano et al. 2008) or by computational prediction of the continuous cell state (Gut et al. 2015; Eulenberg et al. 2017; Rappez et al. 2020; Yang et al. 2020; Szkalicity et al. 2021; Zaritsky et al. 2021; Stallaert et al. 2022; Shakarchy et al. 2024). Notably, the cell’s mitotic state, periphery location, and segmentation were available to us in the AICS dataset used in this study. In “the wild” these cell contexts would be computationally extracted from the raw images.

An alternative approach for incorporating context is through weakly supervised representation-learning, with the cell context as the “weak” label. Previous recent studies guided representations of protein localization patterns using the protein (Kobayashi et al. 2022; Razdaibiedina et al. 2024) or the perturbation (Moshkov et al. 2024) as the weakly supervised label. In principle, cell context can also be used as a label for weakly supervised representation learning. CELTIC’s explicit “injection” of the cell context to the representations has two major benefits. First, the possibility to control the context to morph a specific cell along the context trajectory, while fixing the other factors of cell-cell variability. This

generative capacity along a context trajectory has the potential to serve as a hypothesis generation method to follow how the different organelles and their spatial inter-organelle dependencies are changing as a function of their contexts. The second benefit of explicitly injecting context over weak supervision is technical. There are many possible contexts, and training representations to simultaneously encode multiple weak context labels is not feasible. CELTIC bypasses this limitation by avoiding the technical challenge of learning representations that encode context. Accordingly, the explicit context representation enables learning out-of-distribution label-free images from a very small set of examples consisting of tens of cells per rare population. One advantage of weak supervision is the simpler inference that does not require the weak context label as input.

Context does not improve in silico labeling for all organelles to the same extent. For example, in silico labeling of mitochondria was not improved by much with the inclusion of context indicating that the corresponding brightfield patterns used to localize the mitochondria do not depend much on the cell's context. Systematic characterization of what contexts contribute to the in silico labeling of different cell populations can be used as a phenotypic signature of these populations. Moreover, screening for which contexts contribute the most to the in silico labeling can be used as a method to identify the cell's context. This approach for context prediction is especially relevant for application-appropriate measurements, such as predicting the spindle axis, which should be dramatically improved during mitosis due to the strong association between intracellular organizational patterns and the context. Thus, the same approach can be used to discover unknown patterns that are associated with a specific cell context.

Methods

Data

We used the Allen Institute for Cell Science WTC-11 hiPSC Single-Cell Image Dataset v1. From the field-of-view (FOV) spinning-disk confocal microscopy section, we used the 16-bit Z-stack images, acquired with a 100× objective, with a resolution of 624×924 pixels and a pixel scale of 0.108 micrometers per pixel. Each Z-stack comprised 50–75 slices. Specifically, we used the brightfield channel and the EGFP-tagged cellular structure channel, for the following proteins: alpha-tubulin (microtubules), beta-actin (actin filaments), lamin B1 (nuclear envelope), sec61B (endoplasmic reticulum), STGAL1 (Golgi apparatus), and Tom20 (mitochondria). From the FOV segmentation section, we used the cell segmentation channel (channel 1), an unsigned 8-bit single-channel 3D image showing cell locations within the FOV. Lastly, we used the 'edge_flag' and 'cell_stage' features from the metadata CSV file.

We selected 80 FOV images for training and validation of all the models in this paper (“SET 1”). The images were picked from the list provided in the code repository of (Ounkomol et al. 2018). In cases where images from this list were not available in the single cell dataset, we randomly replaced them with FOV images with comparable cellular properties, such as cell count, mitotic percentage, and edge characteristics. Additionally, we selected 100 FOV images for testing (“SET 2”), based on the same criteria.

In silico labeling replication

We used the original U-Net model provided by (Ounkomol et al. 2018). For training we used 64 images from SET 1 (56 for training, 8 for validation). For testing we used the remaining 16 FOVs of SET 1. We followed the original preprocessing steps, which included resizing the z-slices to 244×366 pixels and normalizing each image to have a mean of 0 and a standard deviation of 1. We report the FOV-based replication results in Table S1.

To analyze cell-level in silico labeling we crop complete single cells from the FOV images of SET 2. We resized the segmentation channel to match the size of the FOV images, without smoothing, to ensure that the label map's indexes remained consistent. We then applied a binary mask to both the predictions and the targets and calculated the Pearson correlation coefficients (PCC) between them, considering only the regions with signal (non-zero values in the mask). We categorized the cells into populations based on the following criteria: Cell Stage (mitosis vs. interphase) by using the metadata cell_stage field,

Edge (interior vs. edge) by using the metadata `edge_flag` field, and Volume, where small cells were those with a volume lower than -1.5 standard deviations from the mean. For neighbor analysis, we examined adjacent voxels and classified cells as having few neighbors if the neighbor count was fewer than 5 (see Methods/Context Representations below for more details). To calculate the p-value, we used the Mann-Whitney U test to compare the small and large populations, with a significance level set at 0.05 (results in Table S2).

Single cell models image preprocessing

We used the FOV cell segmentation label maps to extract individual cells from the FOV images. We excluded partially visible cells due to the lack of metadata for these cells. For each internal cell in the label map, we created a 3D bounding box based on its minimum and maximum x, y, and z values. We then generated binary images where 1 represents the cell area and 0 represents the background, ensuring focused isolation of the cellular content. These bounding boxes and masks were applied to both the brightfield and EGFP FOV images, resulting in a single-cell dataset with each cell represented in two channels: brightfield and EGFP. Pixel intensities of all images were individually normalized to have a mean of 0 and a standard deviation of 1 to account for variations in illumination intensity.

Context Representations

Cell Stage: the representation was extracted from the single-cell metadata CSV file, where the cell cycle stage is indicated as one of six stages: "M0" (interphase), "M1M2" (prophase), "M3" (early prometaphase), "M4M5" (prometaphase/metaphase), "M6M7_single," and "M6M7_complete" (anaphase/telophase/cytokinesis in two stages). This annotation was generated by a deep learning-based classifier and rule-based criteria (Viana et al. 2023). We represented this information numerically as a six-column one-hot vector, with each column corresponding to one of the six cell cycle stages.

Cell Position in the Colony: the representation was extracted from the `edge_flag` column in the single-cell metadata CSV file ('true' for edge cells, 'false' for interior cells). We represented this context as a single boolean variable.

Shape and morphology representations: We employed these two sets of features to provide a comprehensive description of the cell populations. The shape-based representations offered insights into the general dimensions and geometric properties of the cells, allowing for broad classification based on size and shape. The morphology-based features, derived from autoencoder representations, enabled us to capture more subtle and complex attributes, such as intricate structural patterns, which the geometric measurements alone might not fully reveal .

Shape: Using the binary masks of the cells, we calculated the cell height (defined by the minimal and maximal z coordinates within the mask), cell volume (the volume enclosed by the mask), and cell width (the range of sizes along the x and y axes, combined into a single xy axis). Following min-max scaling of these measurements, we applied a k-means classifier to each organelle, determining the optimal number of clusters (k=5) by evaluating the relationship between the number of clusters and the within-cluster sum of squares. Cells were assigned to clusters, represented as one-hot vectors. We also tried using the distances to the k-means centroids but found this to be less effective.

Morphology: We resized the cells' binary masks to images of size [32, 64, 64] for z, y, and x, respectively. An autoencoder was trained on these images, with the encoder consisting of two 3D convolution layers (depths 16 and 32), each followed by ReLU activation and max-pooling with kernel size 2 and stride 2. The decoder included two 3D transposed convolution layers, with ReLU activation for the first and sigmoid activation for the last. The autoencoder was trained for 10 epochs to minimize mean squared error (MSE), on the training set of the endoplasmic reticulum organelle. The latent space of the autoencoder, shaped as [32, 8, 16, 16], was reshaped into vectors of size 65,536. Principal Component Analysis reduced the dimensionality to 5 main components. K-means clustering was then performed, determining the optimal number of clusters (k=3). Shape clusters were represented by cluster membership, with a binary indicator for cluster belongingness.

Number of Neighbors: We used the FOV segmentation images to identify neighboring cells by examining adjacent voxels in the segmentation image. The final count of unique neighboring cells was recorded as the number of neighbors for each cell. These counts were min-max scaled according to the minimum and maximum number of neighbors in the organelle training set.

CELTIC architecture

We adopted the 4-level U-Net architecture inspired by (Ounkomol et al. 2018), incorporating convolutional layers, batch normalization, and ReLU activations. The complete architecture is detailed in Fig. S2. Similar to the original model, which was trained on field-of-view images, we employed patching, as even a single cell in 3D is too large to fit into the GPU. We used patches of size $32 \times 64 \times 64$ (z, y, x), selected randomly from the images. Patches without signal content, due to masking, were discarded. Incorporating additional inputs to access a broader context beyond the given input patch has been shown to be important (Ashesh et al. 2022). We assume that in our case, attaching a global context to each patch helps maintain correlations and preserve spatial context.

Our U-Net model integrates DAFT (Wolf et al. 2022), with the bottleneck producing a feature map (FM) tensor of size $512 \times 2 \times 4 \times 4$, which is input into the DAFT block. The FM undergoes 3D adaptive average

pooling, resulting in a single value per feature map. This tensor is concatenated with the 16-length context vector and encoded by a fully connected layer with a compression rate factor, which is a hyperparameter typically set to 48, followed by a ReLU activation function. A subsequent linear layer decodes the representation to twice the original FM size. Half of this decoded representation is activated by a sigmoid function and used to scale the FM values, while the other half shifts them. The adjusted FM is then propagated through the U-Net's upstream layers. Alternative configurations, where DAFT was applied to different or additional layers, were explored but showed inferior results compared to integrating DAFT at the U-Net bottleneck layer.

CELTIC training and test analysis

To evaluate the contribution of context, we trained and tested models for each organelle dataset, using CELTIC (with the DAFT block and context) and U-NET (without them). For training and validation we used only cell images from SET 1. For reporting the results, we used SET 2.

We randomly split SET 1 into training, validation, and test sets with a ratio of 7:1:2. The split was performed at the FOV level rather than at the single cell level to ensure that cells from a specific FOV are included in only one data split, preventing the models from learning batch effects. The models were trained for 60,000 iterations, using mean squared error (MSE) as the loss function, calculated on the masked signal area. During the training, MSE was measured on the validation set every 100 iterations. To determine the optimal bottleneck size hyperparameter for DAFT, we trained the model using three different split seeds of SET 1. We then selected the bottleneck size that maximized the difference between CELTIC and U-NET on the validation sets. From these three models, we chose the one that best generalized to rare populations in the test sets of SET 1. At the end of this step we obtained six model pairs, one pair per organelle, with each pair consisting of a CELTIC and a U-NET model.

Next, we used the model pairs to predict cell images from SET 2. We calculated the PCC values for cells predicted by CELTIC vs. the same cells predicted by U-NET. We calculated the results for five populations: one population representing all the cells ("All"), and four rare populations (mitosis, edge, small volume, few neighbors). On each population we calculated the delta PCC and the p-value between the models. We used the Wilcoxon signed-rank test. A p-value of 0.05 was considered significant. The p-values, population sizes and distribution of PCC values across organelles and groups is detailed in Table S3.

All training was conducted on an NVIDIA RTX 2080 GPU using PyTorch.

Ablation study

We assessed the contribution of context representation to the *in silico* labeling of rare populations by permuting the context in CELTIC's predictions. For each organelle and rare population, the model's original context was shuffled, one context representation at a time. This shuffling was repeated 10 times for each representation, using different random seeds. The trained model was then used to make predictions on images from SET 2 with permuted context, and the mean Pearson correlation coefficient (PCC) across the shuffles was calculated (Table S4, Fig. S3). These results were compared to the mean PCC obtained using the original context. To evaluate the statistical significance of the differences between the original and shuffled contexts, p-values were calculated, with a paired t-test performed and significance set at $p < 0.05$.

Spindle prediction

We used the brightfield images of all mitotic M4M5 stage (prometaphase/metaphase) cells from the microtubules SET 2 data, totaling 27 cells. We calculated the predictions of the CELTIC and U-NET microtubules model. For segmentation of the predictions, we used the middle z slices of the 3D images, and resized them to 128x128 pixels. We eroded the cell mask with a kernel size of 5 to remove any residual predictions on the cell's border. We then thresholded the prediction into a binary image by masking out values below the 90th percentile. To find the spindle axis, we first identified the contours in the segmented image, retaining the largest two. For each contour, we extracted the moments and calculated the center of mass, then drew a line connecting these centers. If only one contour was present, we drew the longest line that could be feasibly accommodated within the contour. To evaluate metrics against the ground truth spindle, we manually annotated the line over the 27 cells. The location error (ΔC) was calculated as the distance between the two line midpoints. To calculate the orientation error ($\Delta\theta$) we computed the cosine of the angle between the vectors. The permutation test, to determine the significance of $\Delta\theta$, was achieved by performing the $\Delta\theta$ calculation on 250,000 times random shuffles of the ground truth values.

Using context for image generation

We used brightfield images from the endoplasmic reticulum test dataset, and our pre trained *in silico* labeling CELTIC models. To generate cell images with varying contexts, we altered the context representation of the cell. For example, to generate the images in Fig. 5A, we *in silico* labeled an interphase cell with the actin filaments, nuclear envelope and microtubules CELTIC models. The top image is a result of the prediction with the native interphase context. For the bottom result, we

manipulated the cell stage representation in the context vector from M0 (mitotic context = '100000') to M4M5 (000100).

For the quantification analysis (Fig. 5D) we used 16 FOV bright field images from the endoplasmic reticulum that the models did not see before, with a total of 230 single cells. For each image and organelle model, we predicted the in silico labeling using the appropriate context, and then repeated the inference by manipulating the context vector for each non-native context type. We measured the Pearson correlation coefficient between the native prediction and the generated prediction.

Supplementary Information

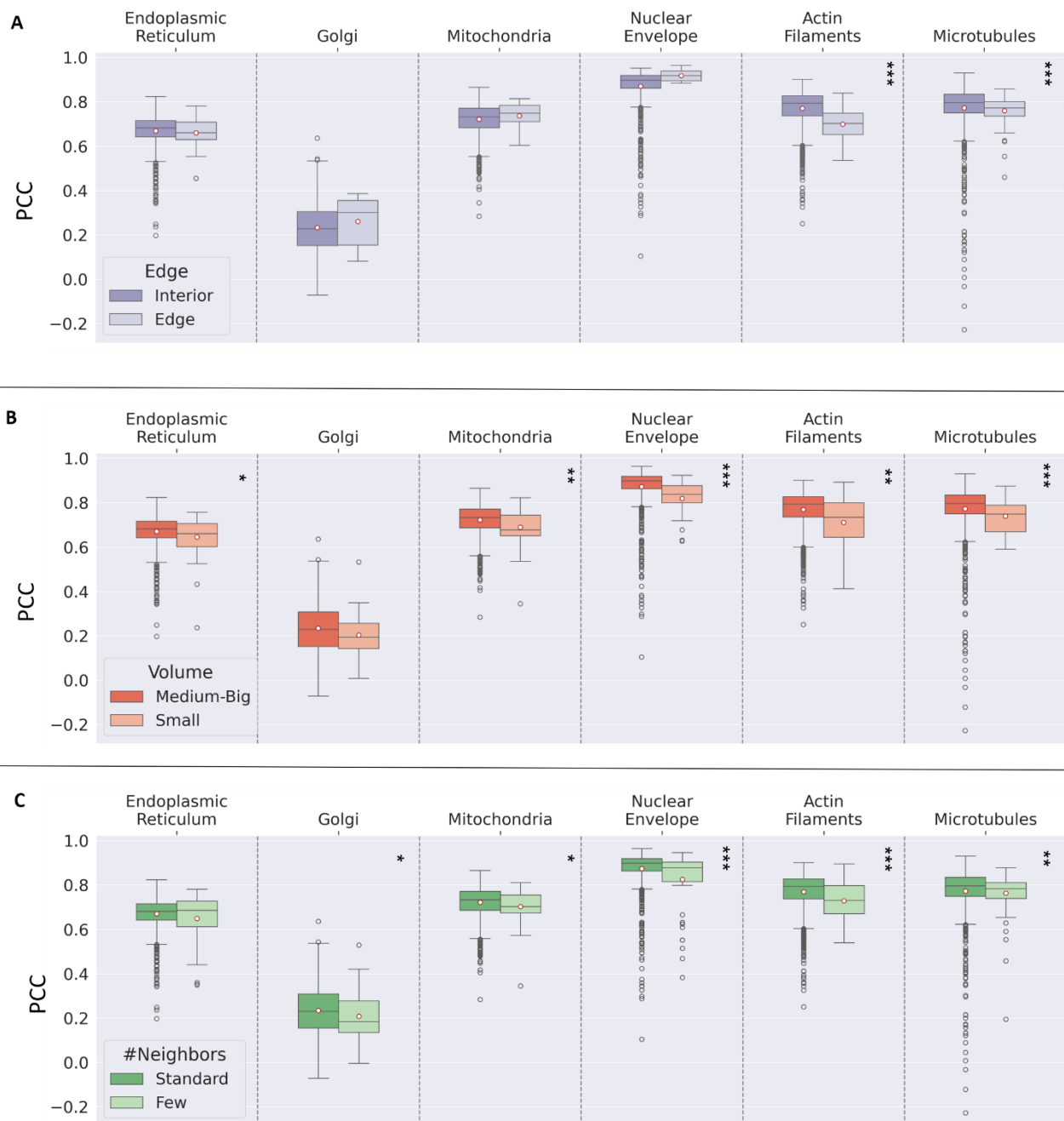


Fig. S1. Distribution of single cell in silico labeling performance across organelles for rare cell populations: (A) location within a the colony (interior versus edge), (B) volume (medium-low vs. small), (C) number of neighbors (standard vs. few). Mann-Whitney U test: * - $p < 0.05$, ** - $p < 0.01$, * - $p < 0.001$. Full results are provided in Table S2.**

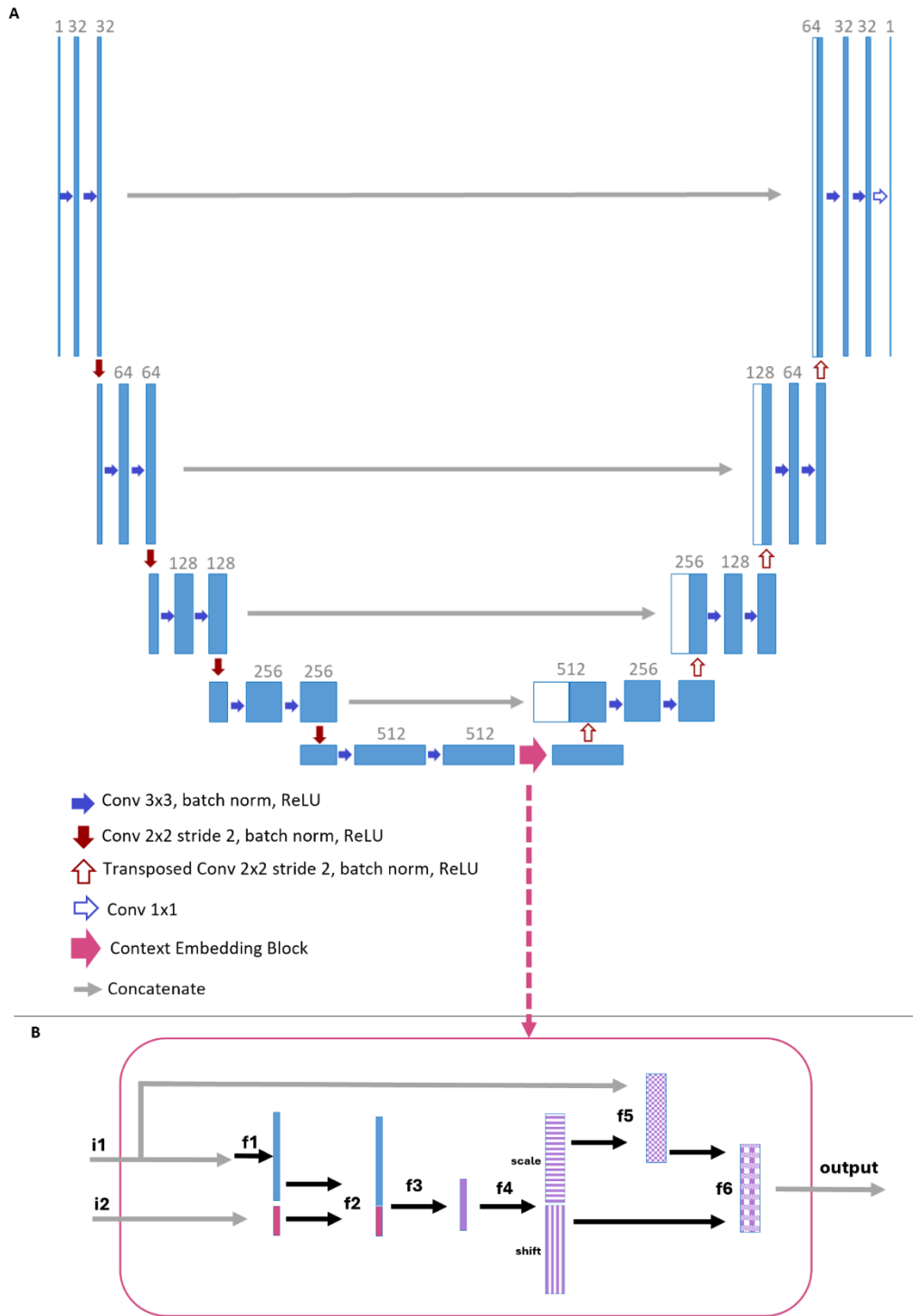


Fig. S2. CELTIC architecture. (A) The U-Net architecture with the CELTIC context embedding block (magenta arrow) adapted from Ronneberger et al. (Ronneberger et al. 2015) cite. (B) Context Embedding Block operation (magenta rectangle) adapted from (Wolf et al. 2022), where i_1 corresponds to the bottleneck feature maps from the U-Net, and i_2 represents the context vector as input. Black arrows illustrate the flow between internal components within the block. The actions are denoted as follows: f_1 - global average pooling; f_2 - concatenation; f_3 - fully connected layer with ReLU activation; f_4 - fully connected layer with post separation for scaling and shifting; f_5 - multiplication of i_1 by the scale, followed by sigmoid activation; f_6 - addition of the shift to the result of f_5 .

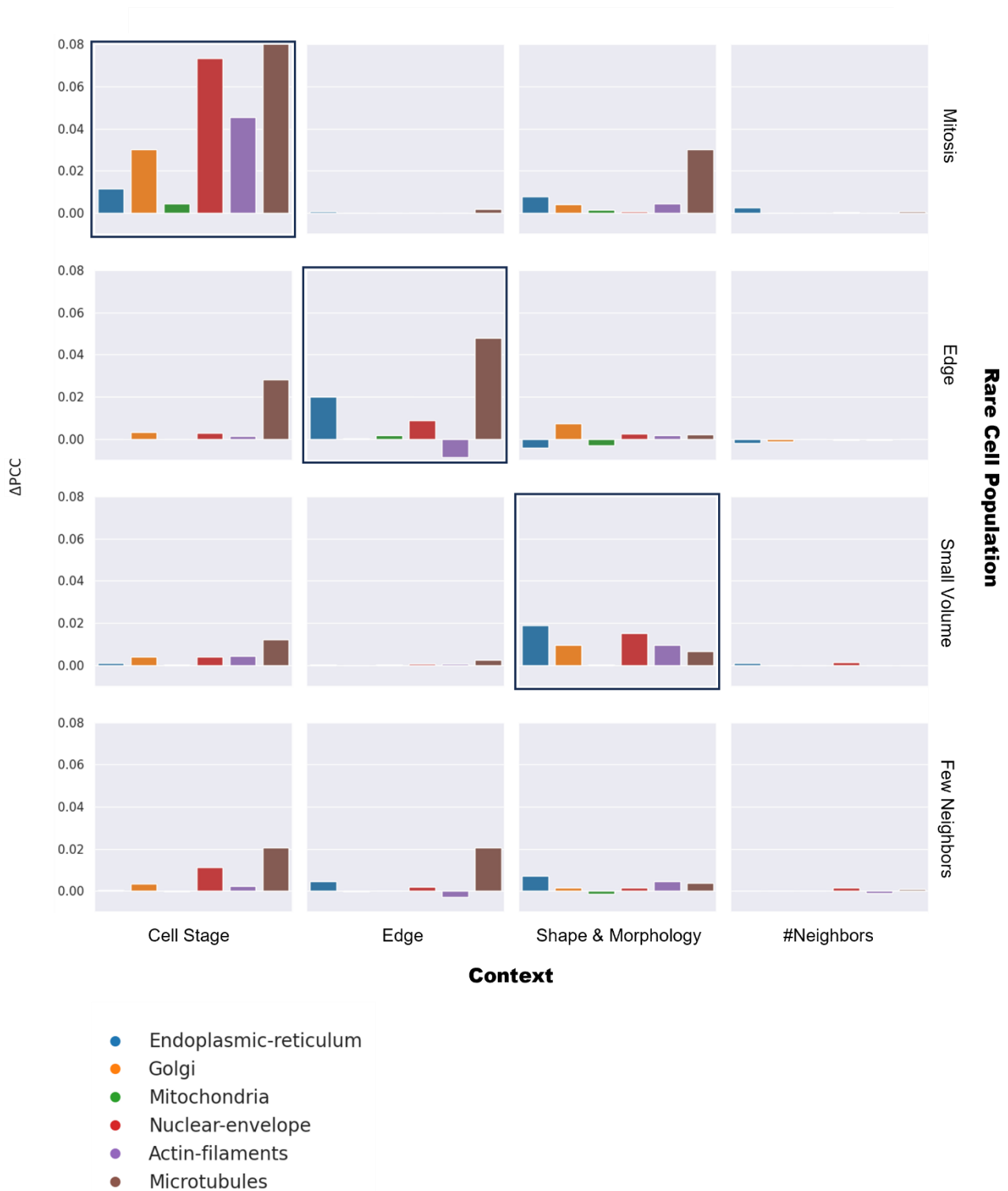


Fig. S3. Ablation study showing the impact of different context types on in silico labeling of rare cell populations. Each row represents a rare cell population, and each column represents a shuffled context type. The bar plots depict the mean Pearson correlation coefficient difference (ΔPCC) between shuffled and non-shuffled contexts, broken down by organelle (color-coded according to the legend). Subplots enclosed in a black box indicate that the rare population is most affected by the CELTIC cell context type relevant to it, for mitosis, edge, and small volumes.

Organelle	Protein	Train-Validation-Test (in number of FOVs)	Iterations	PCC (median)	PCC (mean)
Endoplasmic-reticulum	SEC61B	56-8-16	60,000	0.703	0.709
Golgi	ST6GAL1	56-8-16	60,000	0.225	0.220
Mitochondria	TOMM20	56-8-16	60,000	0.731	0.723
Nuclear-envelope	LMNB1	56-8-16	60,000	0.873	0.872
Actin-filaments	ACTB	56-8-16	60,000	0.774	0.777
Microtubules	TUBA1B	56-8-16	60,000	0.793	0.794

Table S1. Results of replicating the U-Net-based in silico labeling model as reported in (Ounkomol et al. 2018). This table provides a row for each organelle dataset used in the study. Columns (left-to-right): organelle name, the EGFP-tagged protein representing the organelle, the number of field-of-view images used for training-validation-test splitting, the number of model iterations, the median Pearson correlation coefficient on the test set, and the mean Pearson correlation coefficient on the test set.

Protein / Organelle	Tested FOVs / Cells	Category	Population	Cell Count	%	PCC	PCC Diff.	p-value	Significance
SEC61B / Endoplasmic-reticulum	100 / 1191	Cell Stage	Mitosis	52	4.4%	0.534	-	7.10E-18	***
			Interphase	1,139	95.6%	0.676	0.142		
		Edge	Edge	33	2.8%	0.660	-	1.50E-01	
			Interior	1,158	97.2%	0.670	0.010		
Volume	Small	43	3.6%	0.646	-	2.30E-02	*		
	Medium-Big	1,148	96.4%	0.670	0.024				
Neighbours	Few	59	5.0%	0.649	-	2.70E-01			
	Standard	1,132	95.0%	0.671	0.022				
ST6GAL1 / Golgi	100 / 1132	Cell Stage	Mitosis	46	4.1%	0.092	-	1.10E-17	***
			Interphase	1,086	95.9%	0.239	0.147		
		Edge	Edge	21	1.9%	0.261	-	8.90E-02	
			Interior	1,111	98.1%	0.233	0.028		
Volume	Small	23	2.0%	0.203	-	2.40E-02	*		
	Medium-Big	1,109	98.0%	0.234	0.031				
Neighbours	Few	59	5.2%	0.208	-	0.027			
	Standard	1,073	94.8%	0.235	0.027				
TOMM20 / Mitochondria	100 / 1299	Cell Stage	Mitosis	70	5.4%	0.642	-	6.30E-19	***
			Interphase	1,229	94.6%	0.726	0.084		
		Edge	Edge	15	1.2%	0.738	-	5.60E-03	**
			Interior	1,284	98.8%	0.722	0.016		
Volume	Small	35	2.7%	0.689	-	1.50E-02	*		
	Medium-Big	1,264	97.3%	0.723	0.034				
Neighbours	Few	48	3.7%	0.703	-	0.019			
	Standard	1,251	96.3%	0.722	0.019				
LMNB1 / Nuclear-envelope	100 / 1116	Cell Stage	Mitosis	48	4.3%	0.595	-	1.30E-27	***
			Interphase	1,068	95.7%	0.884	0.289		
		Edge	Edge	11	1.0%	0.918	-	1.60E-05	***
			Interior	1,105	99.0%	0.871	0.047		
Volume	Small	22	2.0%	0.820	-	5.70E-04	***		
	Medium-Big	1,094	98.0%	0.873	0.053				
Neighbours	Few	53	4.7%	0.826	-	0.048			
	Standard	1,063	95.3%	0.874	0.048				
ACTB / Actin-filaments	100 / 1575	Cell Stage	Mitosis	76	4.8%	0.586	-	1.20E-35	***
			Interphase	1,499	95.2%	0.778	0.192		
		Edge	Edge	32	2.0%	0.699	-	6.90E-08	***
			Interior	1,543	98.0%	0.770	0.071		
Volume	Small	19	1.2%	0.712	-	8.60E-03	**		
	Medium-Big	1,556	98.8%	0.769	0.057				
Neighbours	Few	49	3.1%	0.729	-	1.20E-05	***		
	Standard	1,526	96.9%	0.770	0.041				
TUBA1B / Microtubules	100 / 1309	Cell Stage	Mitosis	65	5.0%	0.448	-	1.30E-32	***
			Interphase	1,244	95.0%	0.789	0.341		
		Edge	Edge	71	5.4%	0.760	-	3.00E-04	***
			Interior	1,238	94.6%	0.773	0.013		
Volume	Small	30	2.3%	0.740	-	8.50E-04	***		
	Medium-Big	1,279	97.7%	0.773	0.033				
Neighbours	Few	87	6.6%	0.763	-	8.70E-03	**		
	Standard	1,222	93.4%	0.773	0.010				

Table S2. In silico labeling accuracy analysis in rare cell populations. Columns (left to right): organelle dataset, number of field-of-view images / single cells used in the evaluation, rare cell population category, population (with the first row representing the rare population and the second row representing all others), cell count in the population, percentage of the total population, Pearson correlation coefficient of the in silico labeling prediction for each population using the replicated model from (Ounkomol et al. 2018), difference in Pearson correlation coefficient between the rare and non-rare populations (a negative value indicates inferior accuracy of the rare population), calculated p-value between the two populations using the Mann-Whitney U test, and significance levels: $p < 0.05$ (*), $p < 0.01$ (**), and $p < 0.001$ (**).

Organelle	Rare Population	Sample Size	Mean PCC (CELTIC)	Mean PCC (U-NET)	Mean Δ PCC	Std. Δ PCC	p-value	Significance
Endoplasmic-reticulum	All	1,191	0.671	0.665	0.007	0.034	6.62E-17	***
	Mitosis	52	0.537	0.528	0.008	0.064	7.01E-02	
	Edge	33	0.646	0.626	0.020	0.093	2.03E-01	
	Small Volume	43	0.643	0.617	0.026	0.039	3.76E-06	***
	Few Neighbors	59	0.654	0.636	0.018	0.060	6.24E-03	**
Golgi	All	1,132	0.237	0.212	0.025	0.081	8.55E-26	***
	Mitosis	46	0.088	0.061	0.027	0.047	2.52E-06	***
	Edge	21	0.295	0.242	0.054	0.054	1.21E-04	***
	Small Volume	23	0.215	0.200	0.015	0.096	1.65E-01	
	Few Neighbors	59	0.227	0.195	0.032	0.081	2.06E-03	**
Mitochondria	All	1,299	0.713	0.710	0.003	0.026	3.06E-08	***
	Mitosis	70	0.643	0.634	0.009	0.022	7.20E-04	***
	Edge	15	0.716	0.718	-	0.022	6.19E-01	
	Small Volume	35	0.674	0.668	0.006	0.031	1.67E-01	
	Few Neighbors	48	0.691	0.689	0.002	0.029	2.76E-01	
Nuclear-envelope	All	1,116	0.875	0.863	0.012	0.027	5.99E-72	***
	Mitosis	48	0.571	0.534	0.036	0.086	6.16E-03	**
	Edge	11	0.924	0.911	0.013	0.010	2.44E-03	**
	Small Volume	22	0.816	0.788	0.027	0.055	2.71E-02	*
	Few Neighbors	53	0.833	0.811	0.022	0.044	3.59E-05	***
Actin-filaments	All	1,575	0.786	0.788	-	0.023	1.00E+00	
	Mitosis	76	0.652	0.641	0.011	0.037	7.70E-03	**
	Edge	32	0.687	0.688	-	0.024	6.74E-01	
	Small Volume	19	0.763	0.761	0.003	0.026	5.08E-01	
	Few Neighbors	49	0.744	0.744	-	0.023	5.24E-01	
Microtubules	All	1,309	0.787	0.774	0.013	0.086	2.31E-08	***
	Mitosis	65	0.523	0.320	0.203	0.307	3.24E-07	***
	Edge	71	0.757	0.735	0.022	0.042	7.59E-06	***
	Small Volume	30	0.762	0.765	-	0.029	6.94E-01	
	Few Neighbors	87	0.771	0.759	0.011	0.045	1.56E-02	*

Table S3. Comparison of single-cell in silico labeling accuracy between rare populations with context (CELTIC) and without context (U-NET). This analysis was conducted on cells extracted from 100 field-of-view images. Columns (left-to-right): organelle dataset, cell population ('All' indicates the entire population, while other entries represent rare populations), cell count in the population, mean Pearson correlation coefficient with CELTIC, mean Pearson correlation coefficient with U-NET, mean difference (positive values indicate CELTIC's superiority), standard deviation of the difference,

calculated p-value between the two models using the Wilcoxon signed-rank test, and significance levels:
 $p < 0.05$ (*), $p < 0.01$ (**), and $p < 0.001$ (***)).

Organelle	Rare Population	Sample Size	Shuffled Context	Random Shuffles	Mean PCC Without Shuffle	Mean PCC After Shuffle	Δ PCC	p-value	Significance
Endoplasmic-reticulum	Mitotic Cells	52	Cell Stage	10	0.537	0.526	0.012	9.97E-13	***
			Edge	10	0.537	0.536	0.001	5.35E-03	**
			Shape	10	0.537	0.529	0.008	1.33E-05	***
			Neighbors	10	0.537	0.534	0.003	4.27E-06	***
	Edge Cells	33	Cell Stage	10	0.646	0.646	0.000	7.78E-01	***
			Edge	10	0.646	0.626	0.020	2.64E-10	
			Shape	10	0.646	0.650	0.004	9.99E-01	
			Neighbors	10	0.646	0.648	0.002	1.00E+00	
	Small Volume Cells	43	Cell Stage	10	0.643	0.642	0.001	2.71E-02	*
			Edge	10	0.643	0.643	0.000	4.06E-02	*
			Shape	10	0.643	0.624	0.019	6.28E-08	***
			Neighbors	10	0.643	0.642	0.001	0.00E+00	***
	Few Neighbors Cells	59	Cell Stage	10	0.654	0.653	0.001	4.77E-03	**
			Edge	10	0.654	0.649	0.005	1.55E-05	***
			Shape	10	0.654	0.647	0.007	2.62E-07	***
			Neighbors	10	0.654	0.654	0.000	1.72E-01	
Golgi	Mitotic Cells	46	Cell Stage	10	0.088	0.058	0.030	8.07E-13	***
			Edge	10	0.088	0.088	0.000		***
			Shape	10	0.088	0.084	0.004	1.89E-07	***
			Neighbors	10	0.088	0.088	0.000		***
	Edge Cells	21	Cell Stage	10	0.295	0.292	0.003	9.44E-03	**
			Edge	10	0.295	0.295	0.000	8.39E-02	
			Shape	10	0.295	0.288	0.007	3.65E-03	**
			Neighbors	10	0.295	0.296	0.001	1.00E+00	
	Small Volume Cells	23	Cell Stage	10	0.215	0.211	0.004	7.14E-03	**
			Edge	10	0.215	0.215	0.000	6.61E-01	
			Shape	10	0.215	0.205	0.010	1.36E-03	**
			Neighbors	10	0.215	0.215	0.000	9.59E-01	
	Few Neighbors Cells	59	Cell Stage	10	0.227	0.224	0.003	4.47E-03	**
			Edge	10	0.227	0.227	0.000	8.28E-01	
			Shape	10	0.227	0.226	0.002	2.61E-02	*
			Neighbors	10	0.227	0.227	0.000	1.72E-01	
Mitochondria	Mitotic Cells	70	Cell Stage	10	0.643	0.639	0.005	3.18E-10	***
			Edge	10	0.643	0.643	0.000		***
			Shape	10	0.643	0.641	0.002	2.12E-06	***
			Neighbors	10	0.643	0.643	0.000		***
	Edge Cells	15	Cell Stage	10	0.716	0.716	0.000	1.72E-01	

			Edge	10	0.716	0.714	0.002	0.00E+00	***
			Shape	10	0.716	0.719	0.003	9.98E-01	
			Neighbors	10	0.716	0.716	0.000		***
	Small Volume Cells	35	Cell	10	0.674	0.674	0.000	8.39E-02	
			Edge	10	0.674	0.674	0.000	1.72E-01	
			Shape	10	0.674	0.674	0.000	1.35E-01	
			Neighbors	10	0.674	0.674	0.000		***
	Few Neighbors Cells	48	Cell	10	0.691	0.691	0.000	8.28E-01	
			Edge	10	0.691	0.691	0.000		***
			Shape	10	0.691	0.692	0.001	9.93E-01	
			Neighbors	10	0.691	0.691	0.000		***
Nuclear-envelope	Mitotic Cells	48	Cell	10	0.571	0.497	0.074	5.38E-12	***
			Edge	10	0.571	0.571	0.000	5.00E-01	
			Shape	10	0.571	0.570	0.001	2.81E-01	
			Neighbors	10	0.571	0.570	0.001	1.09E-01	
	Edge Cells	11	Cell	10	0.924	0.921	0.003	2.61E-02	*
			Edge	10	0.924	0.915	0.009	0.00E+00	***
			Shape	10	0.924	0.922	0.003	2.24E-05	***
			Neighbors	10	0.924	0.924	0.000	9.82E-01	
	Small Volume Cells	22	Cell	10	0.816	0.812	0.004	5.33E-02	
			Edge	10	0.816	0.815	0.001	1.30E-01	
			Shape	10	0.816	0.801	0.015	8.21E-08	***
			Neighbors	10	0.816	0.815	0.002	4.27E-06	***
	Few Neighbors Cells	53	Cell	10	0.833	0.822	0.011	2.97E-06	***
			Edge	10	0.833	0.831	0.002	0.00E+00	***
			Shape	10	0.833	0.831	0.002	2.50E-05	***
			Neighbors	10	0.833	0.831	0.002	1.40E-07	***
Actin-filaments	Mitotic Cells	76	Cell	10	0.652	0.607	0.046	8.21E-16	***
			Edge	10	0.652	0.652	0.000	8.39E-02	
			Shape	10	0.652	0.647	0.005	1.26E-03	**
			Neighbors	10	0.652	0.652	0.000	8.28E-01	
	Edge Cells	32	Cell	10	0.687	0.685	0.002	3.06E-02	*
			Edge	10	0.687	0.696	0.009	1.00E+00	
			Shape	10	0.687	0.685	0.002	1.36E-02	*
			Neighbors	10	0.687	0.687	0.000	9.82E-01	
	Small Volume Cells	19	Cell	10	0.763	0.759	0.004	1.71E-02	*
			Edge	10	0.763	0.763	0.001	8.86E-02	
			Shape	10	0.763	0.753	0.010	4.39E-05	***
			Neighbors	10	0.763	0.763	0.000	9.03E-01	
	Few Neighbors Cells	49	Cell	10	0.744	0.742	0.002	4.44E-04	***
			Edge	10	0.744	0.747	0.003	1.00E+00	
			Shape	10	0.744	0.739	0.005	5.49E-06	***
			Neighbors	10	0.744	0.745	0.001	9.98E-01	
Microtubules	Mitotic Cells	65	Cell	10	0.523	-0.072	0.595	8.32E-16	***

		Edge	10	0.523	0.521	0.002	9.33E-02	
		Shape	10	0.523	0.493	0.030	2.03E-03	**
		Neighbors	10	0.523	0.522	0.001	1.89E-03	**
Edge Cells	71	Cell						
		Stage	10	0.757	0.729	0.028	3.00E-04	***
		Edge	10	0.757	0.709	0.048	1.22E-13	***
		Shape	10	0.757	0.755	0.002	3.10E-04	***
		Neighbors	10	0.757	0.757	0.000		***
Small Volume Cells	30	Cell						
		Stage	10	0.762	0.750	0.012	2.02E-02	*
		Edge	10	0.762	0.759	0.003	3.13E-03	**
		Shape	10	0.762	0.756	0.006	3.71E-05	***
		Neighbors	10	0.762	0.762	0.000		***
Few Neighbors Cells	87	Cell						
		Stage	10	0.771	0.750	0.021	1.47E-05	***
		Edge	10	0.771	0.750	0.021	7.13E-14	***
		Shape	10	0.771	0.767	0.004	9.61E-06	***
		Neighbors	10	0.771	0.770	0.001	0.00E+00	***

Table S4. Ablation study on the contribution of each context type to in silico labeling of rare populations. Columns (left-to-right): organelle dataset, rare population category, the number of cells in the rare population, the part of the context type from the context input vector that has been shuffled, the number of random shuffles performed, mean Pearson correlation coefficient without shuffling, mean Pearson correlation coefficient with shuffling, difference between non-shuffled and shuffled results (positive values indicate that shuffling deteriorated the in silico labeling), calculated p-value between shuffled and non-shuffled using the t-test, and significance levels: $p < 0.05$ (*), $p < 0.01$ (**), and $p < 0.001$ (***).

References

- Ahmed, R. E., Tokuyama, T., Anzai, T., Chanthra, N., & Uosaki, H. (2022). Sarcomere maturation: function acquisition, molecular mechanism, and interplay with other organelles. *Philosophical Transactions of the Royal Society of London. Series B, Biological Sciences*, 377(1864), 20210325.
- Ashesh, Krull, A., Di Sante, M., Pasqualini, F. S., & Jug, F. (2022). μ Split: efficient image decomposition for microscopy data. In arXiv [cs.CV]. <https://doi.org/10.48550/ARXIV.2211.12872>
- Asmar, A. J., Benson, Z. A., Peskin, A. P., Chalfoun, J., Simon, M., Halter, M., & Plant, A. L. (2024). High-volume, label-free imaging for quantifying single-cell dynamics in induced pluripotent stem cell colonies. *PloS One*, 19(2), e0298446.
- Atwell, S., Waibel, D. J. E., Boushehri, S. S., Wiedenmann, S., Marr, C., & Meier, M. (2023). Label-free imaging of 3D pluripotent stem cell differentiation dynamics on chip. *Cell Reports Methods*, 3(7), 100523.
- Ben-Yehuda, K., Mirsky, S. K., Levi, M., Barnea, I., Meshulach, I., Kontente, S., Benvaish, D., Cur-Cycowicz, R., Nygate, Y. N., & Shaked, N. T. (2022). Simultaneous Morphology, Motility, and Fragmentation Analysis of Live Individual Sperm Cells for Male Fertility Evaluation. *Advanced Intelligent Systems*, 4(4), 2100200.
- Carlton, J. G., Jones, H., & Eggert, U. S. (2020). Membrane and organelle dynamics during cell division. *Nature Reviews. Molecular Cell Biology*, 21(3), 151–166.
- Cheng, S., Fu, S., Kim, Y. M., Song, W., Li, Y., Xue, Y., Yi, J., & Tian, L. (2021). Single-cell cytometry via multiplexed fluorescence prediction by label-free reflectance microscopy. *Science Advances*, 7(3). <https://doi.org/10.1126/sciadv.abe0431>
- Chen, J., Viana, M. P., & Rafelski, S. M. (2023). When seeing is not believing: application-appropriate validation matters for quantitative bioimage analysis. *Nature Methods*, 20(7), 968–970.
- Chen, X., Kandel, M. E., He, S., Hu, C., Lee, Y. J., Sullivan, K., Tracy, G., Chung, H. J., Kong, H. J., Anastasio, M., & Popescu, G. (2023). Artificial confocal microscopy for deep label-free imaging. *Nature Photonics*, 17(3), 250–258.

- Christiansen, E. M., Yang, S. J., Ando, D. M., Javaherian, A., Skibinski, G., Lipnick, S., Mount, E., O'Neil, A., Shah, K., Lee, A. K., Goyal, P., Fedus, W., Poplin, R., Esteva, A., Berndl, M., Rubin, L. L., Nelson, P., & Finkbeiner, S. (2018). In Silico Labeling: Predicting Fluorescent Labels in Unlabeled Images. *Cell*, 173(3), 792–803.e19.
- Cross-Zamirski, J. O., Mouchet, E., Williams, G., Schönlieb, C.-B., Turkki, R., & Wang, Y. (2022). Label-free prediction of cell painting from brightfield images. *Scientific Reports*, 12(1), 10001.
- DAFT: A universal module to interweave tabular data and 3D images in CNNs. (2022). *NeuroImage*, 260, 119505.
- Elmalm, N., Ben Nedava, L., & Zaritsky, A. (2024). In silico labeling in cell biology: Potential and limitations. *Current Opinion in Cell Biology*, 89, 102378.
- Eulenberg, P., Köhler, N., Blasi, T., Filby, A., Carpenter, A. E., Rees, P., Theis, F. J., & Wolf, F. A. (2017). Reconstructing cell cycle and disease progression using deep learning. *Nature Communications*, 8(1), 463.
- Garini, Y., Young, I. T., & McNamara, G. (2006). Spectral imaging: principles and applications. *Cytometry. Part A: The Journal of the International Society for Analytical Cytology*, 69(8), 735–747.
- Gu, S., Lee, R. M., Benson, Z., Ling, C., Vitolo, M. I., Martin, S. S., Chalfoun, J., & Losert, W. (2022). Label-free cell tracking enables collective motion phenotyping in epithelial monolayers. *iScience*, 25(7), 104678.
- Gut, G., Tadmor, M. D., Pe'er, D., Pelkmans, L., & Liberali, P. (2015). Trajectories of cell-cycle progression from fixed cell populations. *Nature Methods*, 12(10), 951–954.
- Heinrich, L., Bennett, D., Ackerman, D., Park, W., Bogovic, J., Eckstein, N., Petruncio, A., Clements, J., Pang, S., Xu, C. S., Funke, J., Korff, W., Hess, H. F., Lippincott-Schwartz, J., Saalfeld, S., Weigel, A. V., & COSEM Project Team. (2021). Whole-cell organelle segmentation in volume electron microscopy. *Nature*, 599(7883), 141–146.
- Icha, J., Weber, M., Waters, J. C., & Norden, C. (2017). Phototoxicity in live fluorescence microscopy, and how to avoid it. *BioEssays: News and Reviews in Molecular, Cellular and Developmental Biology*, 39(8). <https://doi.org/10.1002/bies.201700003>

Ivanov, I. E., Hirata-Miyasaki, E., Chandler, T., Cheloor-Kovilakam, R., Liu, Z., Pradeep, S., Liu, C., Bhave, M., Khadka, S., Arias, C., Leonetti, M. D., Huang, B., & Mehta, S. B. (2024). Mantis: high-throughput 4D imaging and analysis of the molecular and physical architecture of cells. In bioRxiv (p. 2023.12.19.572435). <https://doi.org/10.1101/2023.12.19.572435>

Jo, Y., Cho, H., Park, W. S., Kim, G., Ryu, D., Kim, Y. S., Lee, M., Park, S., Lee, M. J., Joo, H., Jo, H., Lee, S., Lee, S., Min, H.-S., Heo, W. D., & Park, Y. (2021). Label-free multiplexed microtomography of endogenous subcellular dynamics using generalizable deep learning. *Nature Cell Biology*, 23(12), 1329–1337.

Kandel, M. E., He, Y. R., Lee, Y. J., Chen, T. H.-Y., Sullivan, K. M., Aydin, O., Saif, M. T. A., Kong, H., Sobh, N., & Popescu, G. (2020). Phase imaging with computational specificity (PICS) for measuring dry mass changes in sub-cellular compartments. *Nature Communications*, 11(1), 6256.

Kandel, M. E., Kim, E., Lee, Y. J., Tracy, G., Chung, H. J., & Popescu, G. (2021). Multiscale Assay of Unlabeled Neurite Dynamics Using Phase Imaging with Computational Specificity. *ACS Sensors*, 6(5), 1864–1874.

Kobayashi, H., Cheveralls, K. C., Leonetti, M. D., & Royer, L. A. (2022). Self-supervised deep learning encodes high-resolution features of protein subcellular localization. *Nature Methods*, 19(8), 995–1003.

Kroll, J., & Renkawitz, J. (2024). Principles of organelle positioning in motile and non-motile cells. *EMBO Reports*, 25(5), 2172–2187.

LaChance, J., & Cohen, D. J. (2020). Practical fluorescence reconstruction microscopy for large samples and low-magnification imaging. *PLoS Computational Biology*, 16(12), e1008443.

Lee, A., Hirabayashi, Y., Kwon, S.-K., Lewis, T. L., Jr, & Polleux, F. (2018). Emerging roles of mitochondria in synaptic transmission and neurodegeneration. *Current Opinion in Physiology*, 3, 82–93.

Li, H., Habes, M., Wolk, D. A., Fan, Y., & Alzheimer's Disease Neuroimaging Initiative and the Australian Imaging Biomarkers and Lifestyle Study of Aging. (2019). A deep learning model for early prediction of Alzheimer's disease dementia based on hippocampal magnetic resonance imaging data. *Alzheimer's & Dementia: The Journal of the Alzheimer's Association*, 15(8), 1059–1070.

Liu, Z., Hirata-Miyasaki, E., Pradeep, S., Rahm, J., Foley, C., Chandler, T., Ivanov, I., Woosley, H., Lao, T., Balasubramanian, A., Marreiros, R., Liu, C., Leonetti, M., Aviner, R., Arias, C., Jacobo, A., & Mehta, S. B. (2024). Robust virtual staining of landmark organelles. In bioRxiv (p. 2024.05.31.596901). <https://doi.org/10.1101/2024.05.31.596901>

Mati, M. (2015). Prediction of Pathologic Complete Response After Neoadjuvant Chemotherapy in Breast Cancer Patients According to Different Biological Subtypes and Imaging Signs.

Miroshnikova, Y. A., & Wickström, S. A. (2022). Mechanical Forces in Nuclear Organization. *Cold Spring Harbor Perspectives in Biology*, 14(1). <https://doi.org/10.1101/cshperspect.a039685>

Mobadersany, P., Yousefi, S., Amgad, M., Gutman, D. A., Barnholtz-Sloan, J. S., Velázquez Vega, J. E., Brat, D. J., & Cooper, L. A. D. (2018). Predicting cancer outcomes from histology and genomics using convolutional networks. *Proceedings of the National Academy of Sciences of the United States of America*, 115(13), E2970–E2979.

Moshkov, N., Bornholdt, M., Benoit, S., Smith, M., McQuin, C., Goodman, A., Senft, R. A., Han, Y., Babadi, M., Horvath, P., Cimini, B. A., Carpenter, A. E., Singh, S., & Caicedo, J. C. (2024). Learning representations for image-based profiling of perturbations. *Nature Communications*, 15(1), 1594.

Noy, L., Barnea, I., Mirsky, S. K., Kamber, D., Levi, M., & Shaked, N. T. (2023). Sperm-cell DNA fragmentation prediction using label-free quantitative phase imaging and deep learning. *Cytometry. Part A: The Journal of the International Society for Analytical Cytology*, 103(6), 470–478.

Ounkomol, C., Seshamani, S., Maleckar, M. M., Collman, F., & Johnson, G. R. (2018). Label-free prediction of three-dimensional fluorescence images from transmitted-light microscopy. *Nature Methods*, 15(11), 917–920.

Park, J., Bai, B., Ryu, D., Liu, T., Lee, C., Luo, Y., Lee, M. J., Huang, L., Shin, J., Zhang, Y., Ryu, D., Li, Y., Kim, G., Min, H.-S., Ozcan, A., & Park, Y. (2023). Artificial intelligence-enabled quantitative phase imaging methods for life sciences. *Nature Methods*, 20(11), 1645–1660.

Perez, E., Strub, F., De Vries, H., Dumoulin, V., & Courville, A. (2018). FiLM: Visual reasoning with a general conditioning layer. *Proceedings of the ... AAAI Conference on Artificial Intelligence. AAAI Conference on Artificial Intelligence*, 32(1). <https://doi.org/10.1609/aaai.v32i1.11671>

- Plotka, S., Grzeszczyk, M. K., Brawura-Biskupski-Samaha, R., Gutaj, P., Lipa, M., Trzciński, T., Işgum, I., Sánchez, C. I., & Sitek, A. (2023). BabyNet++: Fetal birth weight prediction using biometry multimodal data acquired less than 24 hours before delivery. *Computers in Biology and Medicine*, 167, 107602.
- Pölsterl, S., Sarasua, I., Gutiérrez-Becker, B., & Wachinger, C. (2020). A wide and deep neural network for survival analysis from anatomical shape and tabular clinical data. In *Machine Learning and Knowledge Discovery in Databases* (pp. 453–464). Springer International Publishing.
- Pylvänäinen, J. W., Gómez-de-Mariscal, E., Henriques, R., & Jacquemet, G. (2023). Live-cell imaging in the deep learning era. *Current Opinion in Cell Biology*, 85, 102271.
- Rappez, L., Rakhlin, A., Rigopoulos, A., Nikolenko, S., & Alexandrov, T. (2020). DeepCycle reconstructs a cyclic cell cycle trajectory from unsegmented cell images using convolutional neural networks. *Molecular Systems Biology*, 16(10), e9474.
- Razdaibiedina, A., Brechalov, A., Friesen, H., Mattiazzi Usaj, M., Masinas, M. P. D., Garadi Suresh, H., Wang, K., Boone, C., Ba, J., & Andrews, B. (2024). PIFiA: self-supervised approach for protein functional annotation from single-cell imaging data. *Molecular Systems Biology*, 20(5), 521–548.
- Rickmann, A.-M., Xu, M., Wolf, T. N., Kovalenko, O., & Wachinger, C. (2023). HALOS: Hallucination-free organ segmentation after organ resection surgery. In *Lecture Notes in Computer Science* (pp. 667–678). Springer Nature Switzerland.
- Rivenson, Y., Liu, T., Wei, Z., Zhang, Y., de Haan, K., & Ozcan, A. (2019). PhaseStain: the digital staining of label-free quantitative phase microscopy images using deep learning. *Light, Science & Applications*, 8, 23.
- Rivenson, Y., Wang, H., Wei, Z., de Haan, K., Zhang, Y., Wu, Y., Günaydin, H., Zuckerman, J. E., Chong, T., Sisk, A. E., Westbrook, L. M., Wallace, W. D., & Ozcan, A. (2019). Virtual histological staining of unlabelled tissue-autofluorescence images via deep learning. *Nature Biomedical Engineering*, 3(6), 466–477.
- Ronneberger, O., Fischer, P., & Brox, T. (2015). U-Net: Convolutional Networks for Biomedical Image Segmentation. *Medical Image Computing and Computer-Assisted Intervention: MICCAI ... International Conference on Medical Image Computing and Computer-Assisted Intervention*, 234–241.

Sakaue-Sawano, A., Kurokawa, H., Morimura, T., Hanyu, A., Hama, H., Osawa, H., Kashiwagi, S., Fukami, K., Miyata, T., Miyoshi, H., Imamura, T., Ogawa, M., Masai, H., & Miyawaki, A. (2008). Visualizing spatiotemporal dynamics of multicellular cell-cycle progression. *Cell*, 132(3), 487–498.

Shakarchy, A., Zarfati, G., Hazak, A., Mealem, R., Huk, K., Ziv, T., Avinoam, O., & Zaritsky, A. (2024). Machine learning inference of continuous single-cell state transitions during myoblast differentiation and fusion. *Molecular Systems Biology*, 20(3), 217–241.

Somani, A., Ahmed Sekh, A., Opstad, I. S., Birna Birgisdottir, Å., Myrmel, T., Singh Ahluwalia, B., Horsch, A., Agarwal, K., & Prasad, D. K. (2022). Virtual labeling of mitochondria in living cells using correlative imaging and physics-guided deep learning. *Biomedical Optics Express*, 13(10), 5495–5516.

Stallaert, W., Kedziora, K. M., Taylor, C. D., Zikry, T. M., Ranek, J. S., Sobon, H. K., Taylor, S. R., Young, C. L., Cook, J. G., & Purvis, J. E. (2022). The structure of the human cell cycle. *Cell Systems*, 13(3), 230–240.e3.

Sullivan, D. P., & Lundberg, E. (2018). Seeing More: A Future of Augmented Microscopy. *Cell*, 173(3), 546–548.

Szkalisity, A., Piccinini, F., Beleon, A., Balassa, T., Varga, I. G., Migh, E., Molnar, C., Paavolainen, L., Timonen, S., Banerjee, I., Ikonen, E., Yamauchi, Y., Ando, I., Peltonen, J., Pietiäinen, V., Honti, V., & Horvath, P. (2021). Regression plane concept for analysing continuous cellular processes with machine learning. *Nature Communications*, 12(1), 2532.

Tonks, S., Nguyen, C., Hood, S., Musso, R., Hopely, C., Titus, S., Doan, M., Styles, I., & Krull, A. (2024). Can virtual staining for high-throughput screening generalize? <http://arxiv.org/abs/2407.06979>

Valm, A. M., Cohen, S., Legant, W. R., Melunis, J., Hershberg, U., Wait, E., Cohen, A. R., Davidson, M. W., Betzig, E., & Lippincott-Schwartz, J. (2017). Applying systems-level spectral imaging and analysis to reveal the organelle interactome. *Nature*, 546(7656), 162–167.

Viana, M. P., Chen, J., Knijnenburg, T. A., Vasan, R., Yan, C., Arakaki, J. E., Bailey, M., Berry, B., Borensztein, A., Brown, E. M., Carlson, S., Cass, J. A., Chaudhuri, B., Cordes Metzler, K. R., Coston, M. E., Crabtree, Z. J., Davidson, S., DeLizo, C. M., Dhaka, S., ... Rafelski, S. M. (2023). Integrated intracellular organization and its variations in human iPS cells. *Nature*, 613(7943), 345–354.

Wang, R., Butt, D., Cross, S., Verkade, P., & Achim, A. (2023). Bright-field to fluorescence microscopy image translation for cell nuclei health quantification. *Biological Imaging*, 3, e12.

Wang, Z., Xie, Y., & Ji, S. (2021). Global voxel transformer networks for augmented microscopy. *Nature Machine Intelligence*, 3(2), 161–171.

White, A., Saranti, M., d'Avila Garcez, A., Hope, T. M. H., Price, C. J., & Bowman, H. (2024). Predicting recovery following stroke: Deep learning, multimodal data and feature selection using explainable AI. *NeuroImage. Clinical*, 43, 103638.

Wolf, T. N., Pölsterl, S., Wachinger, C., Alzheimer's Disease Neuroimaging Initiative, & Australian Imaging Biomarkers and Lifestyle flagship study of ageing. (2022). DAFT: A universal module to interweave tabular data and 3D images in CNNs. *NeuroImage*, 260, 119505.

Yamashita, Y. M. (2009). Regulation of asymmetric stem cell division: spindle orientation and the centrosome. *Frontiers in Bioscience*, 14(8), 3003–3011.

Yang, K. D., Damodaran, K., Venkatachalapathy, S., Soylemezoglu, A. C., Shivashankar, G. V., & Uhler, C. (2020). Predicting cell lineages using autoencoders and optimal transport. *PLoS Computational Biology*, 16(4), e1007828.

Ye, Z., Hu, C., Wang, J., Liu, H., Li, L., Yuan, J., Ha, J. W., Li, Z., & Xiao, L. (2023). Burst of hopping trafficking correlated reversible dynamic interactions between lipid droplets and mitochondria under starvation. *Exploration (Beijing, China)*, 3(5), 20230002.

Zaritsky, A., Jamieson, A. R., Welf, E. S., Nevarez, A., Cillay, J., Eskiocak, U., Cantarel, B. L., & Danuser, G. (2021). Interpretable deep learning uncovers cellular properties in label-free live cell images that are predictive of highly metastatic melanoma. *Cell Systems*, 12(7), 733–747.e6.

תקציר

חיזוי אין סליקו של פלואורסנציה של אברונים מתוך תמונות מיקרוסקופיה לא מתוייגות יכול לשנות את ההבנה שלנו לגבי תאים כמערכות מורכבות משולבות. עם זאת, שינויים בארגון התא במהלך תהליכים ושיבושים ביולוגיים עשויים להוביל לשינויים בתמונות הלא מתוייגות ולפגוע בביצועי החיזוי. הדגמנו כי שילוב הקשרים הביולוגיים המשמעותיים של התאים, באמצעות מודל תלוי הקשר שאנו מכנים "סלטיק", שיפר את החיזוי ואיפשר ביצוע של ניתוחים נוספים של אוכלוסיות תאים שמחוץ להתפלגות, כגון תאים העוברים חלוקה ותאים הממוקמים בקצה המושבה. תוצאות אלו מצביעות על קשר בין הקשר התאים לבין הארגון התוך-תאי. השימוש בסלטיק לביצוע תמורה גנרטיבית של תאים בודדים העוברים שינוי בהקשר, אפשר איפיון משולב של השינויים ההדרגתיים בארגון התאי בין אברונים שונים, תוך התגברות על השונות בין התאים. הכללת ההקשר באופן מפורש יכולה להביא להרמוניזציה של בסיסי נתונים, ולסלול את הדרך למודלי יסוד כלליים לתיוג אין סליקו.



אוניברסיטת בן-גוריון בנגב
הפקולטה למדעי ההנדסה
המחלקה להנדסת מערכות תוכנה ומידע

**לוקליזאציה של אברונים אין-סיליקון מבוססת הקשר תאי
בתמונות מיקרוסקופיה לא מתוייגות**

חיבור זה מהווה חלק מהדרישות לקבלת תואר מגיסטר בהנדסה

ניצן אלמלם

בהנחיית פרופ' אסף זריצקי

ספטמבר 2024



אוניברסיטת בן-גוריון בנגב
הפקולטה למדעי ההנדסה
המחלקה להנדסת מערכות תוכנה ומידע

**לוקליזאציה של אברונים אין-סיליקון מבוססת הקשר תאי
בתמונות מיקרוסקופיה לא מתוייגות**


חיבור זה מהווה חלק מהדרישות לקבלת תואר מגיסטר בהנדסה

ניצן אלמלם

בהנחיית פרופ' אסף זריצקי

20.09.2024

20.09.2024





חתימת המחבר :

אישור המנחה :

אישור יו"ר ועדת תואר שני מחלקתית

ספטמבר 2024